Improved cloudy-sky snow surface albedo estimates using passive microwave and VIIRS data

Aolin Jia[a], Dongdong Wang[a,*], Shunlin Liang[b], Jingjing Peng[c,d], and Yunyue Yu[c]

[a] Department of Geographical Sciences, University of Maryland, College Park, MD, 20742, USA

[b] Department of Geography, The University of Hong Kong, Hong Kong, 999077, China

[c] NOAA/NESDIS Center for Satellite Application and Research, College Park, MD 20742, USA

[d] Earth System Science Interdisciplinary Center, University of Maryland, College Park, MD, 20742, USA

**Correspondence to*: Dongdong Wang (ddwang@umd.edu)

Highlights

- Novel method for cloudy-sky albedo estimation involving passive microwave and climatological data
- Higher accuracy of 1 km cloudy-sky albedo compared to other methods (especially in snow)
- Significantly improved performance for capturing ephemeral snow events under clouds

Abstract

Land surface albedo (LSA) is an essential component of the surface radiation budget, and has been retrieved extensively as a basic remote sensing product; however, daily LSA products suffer from extensive data gaps primarily caused by cloud cover. Accordingly, several gap-filling methods were developed (e.g., spatiotemporal interpolation and data fusion with albedo climatology), although the traditional methods are limited by cloud scale and surface heterogeneity. Further, as the largest varying surface landscape feature, seasonal snow cover substantially influences LSA and represents a major uncertainty factor of gap recovery because previous studies failed to employ actual surface signals to capture such ephemeral but intense albedo changes under cloud cover. To address this issue, a three-step framework was proposed for estimating 1 km cloudy-sky LSA using passive microwave (PMW) data, albedo climatology, and Visible Infrared Imaging Radiometer Suite (VIIRS) clear-sky albedo: 1) All-sky snow albedo was estimated from PMW brightness temperatures using a statistical model, 2) Continuous albedo dynamics were generated by combining the all-sky snow albedo with snow-free climatological albedo, and 3) The 1 km cloudy-sky LSA was predicted after filtering 1 km VIIRS clear-sky LSA by the albedo dynamic series. PMW-derived snow albedo was assessed over the Contiguous US (CONUS), and the final 1 km cloudy-sky LSA was validated across 10 sites from SURFRAD and Core AmeriFlux in 2013. Based on the comparison with high-quality MODIS pixels, the estimated snow albedo yielded an overall RMSE of 0.064 over CONUS, with a bias of -0.010 ($R^2 = 0.845$). The recovered 1 km cloudy-sky LSA produced RMSEs of 0.074 (0.137) for all (snow) samples, a significant improvement over the Global Land Surface Satellite (GLASS) gap-free albedo products especially on snow cases (p-value = 0.027). Corresponding RMSE in calculating surface net radiation was also decreased by 38.91 $W \cdot m^{-2}$; and anomalous snow samples were corrected as well. The temporal analysis and all-sky LSA mapping suggest that the recovered LSA has satisfactory spatiotemporal continuity, and successfully captured details of spatiotemporal variability, especially for ephemeral snow events. This study provides an innovative solution to recover gaps in LSA data, and considerably improves the LSA accuracy under cloud cover, which can inform snow melting modeling, hazard forecasting, and irrigation management.

Keywords: land surface albedo, gap filling, VIIRS, passive microwave, snow

1 Introduction

Land surface albedo (LSA) is defined as the fraction of reflected surface shortwave radiation flux among total incident shortwave radiation (Trenberth et al., 2009), and is a critical surface radiation component that characterizes the reflective ability of land surfaces towards solar energy (Liang et al., 2010). Accordingly, it is considered an Essential Climate Variable (GCOS, 2004), and determines the surface energy balance and partitioning of general circulation (Heldens et al., 2017; Lawrence et al., 2019) and biophysical models (Anderson et al., 2011), as well as providing important data for hydrological budget monitoring (Chen and Liu, 2020; Jiang et al., 2019) and weather forecasting (Boussetta et al., 2015). LSA can be obtained by ground measurement, model simulation, and satellite retrieval (Gueymard et al., 2019); however, considering the high spatiotemporal heterogeneity of LSA impacted by land cover and soil types (Davidson and Wang, 2004; He et al., 2019), vegetation phenology (Rechid et al., 2009), soil moisture (Guan et al., 2009), deposited soot and absorbing aerosol (Jia et al., 2020; Zhang et al., 2019a), flooding and wildfire (Huang et al., 2013; San Jose et al., 2001), etc., satellite retrieval remains the only practical approach for accurately monitoring global LSA.

Satellite-derived LSA datasets have been extensively developed (Qu et al., 2015), including for the Moderate Resolution Imaging Spectroradiometer (MODIS) (Schaaf et al., 2011; Schaaf et al., 2002), Visible Infrared Imaging Radiometer Suite (VIIRS) (Wang et al., 2013), Advanced Very-High-Resolution Radiometer (AVHRR) (Karlsson et al., 2013; Liang et al., 2013), and Landsat (He et al., 2018). Although these global LSA products are easily accessible, they suffer from data gaps, primarily due to cloud cover, sensor malfunction, and orbital discontinuities. For example, one analysis of 12 yr MODIS data suggested that cloud cover over global land can reach 55% (King et al., 2013). Compared to the high surface heterogeneity, clouds severely restrict the application of the LSA products. Consequently, numerous studies have focused on LSA reconstruction and related satellite data gap-filling (Gerber et al., 2018; Shen et al., 2015; Yan and Roy, 2018), either through pre-processing with the Bidirectional Reflectance Distribution Function (BRDF) coefficients and nadir BRDF adjusted reflectance (Ju et al., 2010; Muller et al., 2012; Samain et al., 2006), or post-processing of LSA imagery (Fang et al., 2007; Jääskeläinen et al., 2022; Liu et al., 2013a; Shuai et al., 2014). Based on input sources, these image reconstruction methodologies can be divided into three categories: data interpolation, data filtering using prior knowledge, and data fusion from multiple sensors.

Interpolation-based methods reconstruct image gaps by applying the information only from temporally, spatially, or spatiotemporally adjacent non-missing pixels (Yan and Roy, 2020). Temporal interpolation generates a statistical time series model fit by neighboring clear-sky samples, such as the harmonic analysis of time-series (HANTS) (Roerink et al., 2000), spline interpolation (Sharifi et al., 2019), and temporal Fourier analysis (Scharlemann et al., 2008); however, accuracy is considerably affected by the temporal window size and cloud duration. Based on the spatial autocorrelation, missing pixels can be also filled by spatial interpolation, such as with inverse distance weighted (Tomar et al., 2014) and Kriging interpolation (Yang and Hu, 2018). Nevertheless, accuracy here depends on the spatial distribution of reference pixels and surface heterogeneity. Moreover, spatiotemporal interpolations can incorporate both texture and temporal variation around missing values, such as spatiotemporal Savitzky-Golay interpolation (Cao et al., 2018), nonnegative matrix factorization (Li et al., 2019b), and spatiotemporal tensor completion (Chu et al., 2021). Still, image spatial textures are not easily reconstructed when the scale of cloud cover is substantial (Wu et al., 2011). Subsequently, to fully extract spatiotemporally adjacent information, machine learning (ML)-based methods have been developed to deal with this issue and fill missing values for large cloudy regions (Sarafanov et al., 2020; Wang et al., 2022; Wu et al., 2019; Zhang et al., 2020a; Zhang et al., 2018). Although these methods are effective for maintaining image texture, they cannot capture ephemeral albedo disturbance without the accurate acquisition of signals under clouds (e.g., snowfall and melting), as such considerable albedo variation caused by snow could be mostly hidden, leaving reconstructed LSA with considerable bias. Further, the feasibility of ML-based models is limited by the quality and quantity of training samples. In addition, the statistical models mentioned above may not be properly constrained by physical relationships, such as the impacts of vegetation phenology on LSA (He et al., 2014; Jia et al., 2022c).

Missing pixels can be predicted and physically constrained by filtering discontinuous clear-sky data series based on prior knowledge, such as albedo climatology, ecosystem-dependent phenological profiles, and corresponding simulated series from physical models. Albedo climatology is the continuous annual series generated by averaging albedo records across multiple years for each day of year (DOY), thereby representing general albedo variation at the climatological scale for each pixel (Jia et al., 2022c). By filtering real-time retrievals of clear-sky days using the climatological information, gaps in the data can be accurately predicted (Fang et al., 2007; Liu et al., 2013a; Xiao et al., 2011). Ecosystem curve fitting methods have been proposed to generate continuous MODIS albedo products based on vegetation phenology (Moody et al., 2005; Samain et al., 2006). Such phenological curve fitting studies typically combine neighboring years of clear-sky samples into a single-year period for decreasing the fitting uncertainty (Kennedy et al., 2010; Rufin et al., 2019), as this prior knowledge can restrict predictions using physical correlations of albedo change with vegetation phenology; however, it still cannot confidently reflect real-time variation under clouds without introducing actual surface information, especially the substantial albedo change caused by snow. In comparison, model simulations continuously estimate real-time land surface and atmospheric interactions, clear-sky satellite retrievals can be filtered correspondingly via continuous simulations of temporal (Jia et al., 2021) or spatiotemporal data series (Jia et al., 2022a); nevertheless, the recovery accuracy is considerably affected by simulation uncertainty on cloudy days, especially at higher elevation regions.

As the largest varying landscape features of the Earth's surface, snow cover is a predominant driving factor of LSA variations, and it is also a primary source of error for current reconstruction methodologies due to the distinct albedo difference with or without snow coverage (Moreno-Martinez et al., 2020). Previous reconstruction studies either only focused on snow-free conditions (Ju et al., 2010; Shuai et al., 2014), or produced considerable errors under snow-covered conditions. For example, cloudy-sky snow albedo has a root mean square error (RMSE; i.e., accuracy) of 0.198, substantially higher than snow-free reconstruction results (RMSE = 0.073) (Fang et al., 2007). Besides, most seasonal snow albedo samples were not captured by comparing reconstructed results with ground measurements in spring and fall (Liu et al., 2013a; Liu et al., 2013b), resulting in bias greater than 0.13 (Urraca et al., 2022). The uncertainty is mainly because ephemeral snow is easily hidden under cloud cover, and such seasonal snow cover disturbance is difficult to be obtained only based on interpolation and climatology. The large uncertainties of snow albedo lead to ‘cold bias’ (−3 to −11 °C) of simulated surface air temperature at the Tibetan plateau (Meng et al., 2018), and ultimately affect the Asian monsoon system modeling.

Accordingly, it is urgent to improv snow albedo estimation under clouds by incorporating actual snow signals.

Passive microwave radiometers (PMW) can penetrate clouds, and have shown their capacity to characterize land surface variations under cloud cover (Abdalati and Steffen, 1997). Data fusion of clear-sky optical retrievals and all-sky PMW retrievals has become an important method for generating gap-free high-resolution images of surface variables, such as snow cover extent (Li et al., 2019a; Metsämäki et al., 2015), land surface temperatures (Wu et al., 2022; Xu and Cheng, 2021; Zhang et al., 2019b), soil moisture (Cui et al., 2016; Sabaghy et al., 2018), and sea ice albedo (Laine et al., 2011; Pistone et al., 2014). To the best of the authors' knowledge, few studies have focused on improving cloudy-sky snow albedo estimation by involving PMW data. Indeed, it has been shown that variations in snow can be observed through PMW radiometers that are capable of recording the scattering information caused by surface snow physical properties, such as snow depth, density, and grain size (COMET, 2015), and presence of melting (Foster et al., 1984). PMW data represent an important data source for retrieving snow cover and snow water equivalent (SWE) (Foster et al., 2005; Luojus et al., 2021; Mortimer et al., 2020; Vander Jagt et al., 2013). SWE is a widely used measurement of snow amount, and a decisive parameter for calculating snow cover fractions and albedo in land surface models based on snow depletion curves (Essery and Pomeroy, 2004), such as the Noah model (Barlage et al., 2010), biosphere-atmosphere transfer scheme (BATS) model (Yang et al., 1997), simple biosphere (SiB) model (Sellers et al., 1996), and Goddard Institute of Space Studies (GISS) model (Hansen et al., 1983). Therefore, the snow depletion curve indicates that SWE and snow depth highly correlate with LSA before snow fully covers the ground (generally when snow depth is $\leqslant$ 20 cm, e.g., ephemeral snow) (Chen et al., 2014). Accordingly, emerging studies have utilized PMWs for retrieving snow cover fraction, a direct component determining snow albedo value (Kostadinov et al., 2019; Xiao et al., 2021a; Xiao et al., 2021b). Based on the short revisit period of PMW data, and its clear physical relationship with SWE and snow fraction (Bair et al., 2019; Pan et al., 2015; Xue et al., 2014), it maintains strong potential for characterizing snow albedo dynamics under clouds as well (Painter et al., 2016).

In order to improve the cloudy-sky LSA accuracy affected by snow cover, in this study, a three-step framework was developed using the PMW brightness temperatures (BTs), albedo climatology, and clear-sky LSA retrievals: 1) The all-sky snow LSA was retrieved from PMW BTs using a statistical model; 2) By combining the all-sky snow LSA with snow-free albedo climatological data, continuous albedo dynamic series were generated as prior knowledge, and considered as the first estimate of all-sky LSA; and, 3) To correct prior knowledge for fitting real-time conditions, a spatiotemporal filtering method was implemented to fuse available clear-sky VIIRS albedo, with the albedo dynamic series, allowing for the 1 km LSA under clouds to be recovered.

The proposed framework here was implemented over the Contiguous United States (CONUS) using blue-sky daily VIIRS albedo, and calibrated resolution-enhanced Special Sensor Microwave Imager/Sounder (SSMIS) BTs. The novelty of this research stems from its: 1) Recovery of cloudy-sky LSA by incorporating both actual observations under clouds, and prior knowledge from albedo climatology; 2) Substantial improvement in estimation accuracy of cloudy-sky snow albedo compared with existing albedo products, especially for ephemeral snow cover; 3) Suggestion that this framework is sensor-independent, and feasible across various regions; and 4) Capacity to decrease uncertainty when quantifying surface energy budgets on cloudy days, which is critical to snow cover and melting modeling (Kumar et al., 2020; Xu and Shu, 2014), irrigation management (Wang et al., 2014), flood forecasting (Bryant et al., 2013), extreme weather assessments (Guan et al., 2010).

2 Data and methods

2.1 Data

2.1.1 MODIS surface albedo product

The MODIS Daily 0.05° shortwave surface albedo (MCD43C3) from 2015 to 2019 was sampled as the response variable during snow albedo model training. MODIS albedo was estimated from a semi-empirical linear kernel-driven model (Lucht et al., 2000), with > 20 years of accumulated data with high accuracy (Lawrence and Chase, 2007; Li et al., 2016); thus, it has been employed as the training label in numerous studies (Cho et al., 2022; Xiao et al., 2021a). Blue-sky albedo is calculated using black-sky albedo (BSA) and white-sky albedo (WSA) from MCD43C3, where the 0.55 μm aerosol optical depth (AOD) from MOD08 was utilized to assign weights to BSA and WSA (Jia et al., 2022c). Snow samples were included for training and evaluation only if the BRDF quality was "best", and the "percent inputs" was 100%. Further, due to computational resource limitations, snow albedo from 2015 to 2019 (the period was randomly selected) was sampled over CONUS for constructing the statistical model, and the predictions were evaluated for 2013, the year when VIIRS LSA was offline produced for algorithm test.

2.1.2 Interactive Multisensor Snow and Ice Mapping System (IMS) snow mask

IMS all-sky binary snow mask from the National Oceanic and Atmospheric Administration (NOAA) was utilized to classify snow and snow-free pixels. The IMS snow mask is generated by fusing optical, infrared, and PMW satellite data, as well as ground measurements (Helfrich et al., 2007; Ramsay, 1998). The daily rate of agreement between IMS and site measurement mostly ranges between 80% and 90% (Chen et al., 2012), which meets the requirement for generating new datasets, such as seasonal melt duration/ice cover duration (Brown et al., 2014). It has been selected as the reference snow mask for reanalysis datasets (Dee et al., 2011; Muñoz-Sabater et al., 2021), VIIRS series satellite product production (Peng et al., 2020), and other product assessments (Chiu et al., 2020; Hall et al., 2019; Orsolini et al., 2019). Here, only samples of snow days were utilized for the snow albedo model training and prediction.

2.1.3 PMW observations

As essential independent variables of snow albedo estimates, PMW observations typically maintain a coarse spatial resolution (> 0.1 °), which does not align with the optical LSA products. To address this limitation, the Calibrated Enhanced-Resolution Passive Microwave Daily Equal-Area Scalable Earth Grid (EASE-Grid) 2.0 BTs, released by the Making Earth System Data Records for Use in Research Environments (MEaSUREs) from NASA, were employed, as they represent an improved, enhanced-resolution, daily PMW dataset for monitoring cryospheric and hydrologic long-term dynamics from Scanning Multichannel Microwave Radiometer (SMMR), SSMIS, and the Advanced Microwave Scanning Radiometer-Enhanced (AMSE) (Brodzik et al., 2018). MEaSUREs project reconstructed the original spatial resolution by the effective measurement response function (MRF), and gridded the observations according to the “drop-in-the-bucket” average algorithm (Brodzik and Long, 2018). This calibrated dataset has previously been used for mapping high resolution snow parameters (Meloche et al., 2022; Mortimer et al., 2022; Pan et al., 2020; Xiao et al., 2021a). Three channels (19, 37, and 91 GHz) of SSMIS (F18), in both horizontal (*H*) and vertical (*V*) polarization from descending orbit (morning) were used here. Notably, 22 GHz was not included due to its high sensitivity to atmospheric water vapor

(Liljegren et al., 2005). The spatial resolution of 37 and 91 GHz was aggregated from 3.125 km to 6.25 km (~ 0.05 °) to align with the 19 GHz data in Climate Modeling Grid (CMG). It should be noted that PMW data have swath gaps at lower latitudes due to their limited scanning widths. As the temporal duration of such swaths only lasts for a single day in a specific location (Zhang et al., 2020b), temporal linear interpolations were used to fill gaps in the data based on observations from the previous and following days. As snow events primarily occur at mid- and high-latitudes, this simple approach was expected to have minimal impacts on the overall results.

2.1.4 All-sky land surface temperature (LST)

All-sky LST was an additional independent variable for snow albedo estimation. PMW signals depend on the amount of scattering and attenuation by the snowpack, while longwave emissions from the land surface below the snowpack can also substantially influence the final BTs received by satellites. Accordingly, LST is commonly required to accurately interpret PMW signals for SWE estimates (COMET, 2015; Hancock et al., 2013). Simultaneously, snow falling and melting also control LST variations (Meng et al., 2018; Thiebault and Young, 2020); thus, the all-sky hourly LST over the CONUS was generated by fusing clear-sky hourly retrievals from the Copernicus Global Land Service (Freitas et al., 2013) with ERA5 LST, while the reconstructed LST during cloud periods was further corrected using satellite radiation products based on the surface energy balance (SEB) equation (Jia et al., 2022a; Jia et al., 2022b). Therefore, meteorological reanalysis information was also used in the study. The all-sky LST was extracted according to the PMW passing time.

2.1.5 Surface albedo climatology

Snow-free albedo climatology was employed to generate continuous albedo dynamics with PMW snow albedo, which was ultimately used to filter VIIRS clear-sky retrievals for predicting cloudy-sky LSA. Snow-free albedo climatology reflects general albedo variation primarily due to local vegetation phenology. By combining all-sky snow albedo from PMW, and snow-free albedo climatology, a continuous albedo dynamic series can be generated for characterizing the phenology-constrained LSA variation, and actual albedo disturbance due to snowfall and melting. Here, snow-free albedo climatology was calculated using Google Earth Engine by averaging 20-year snow-free MODIS blue-sky albedo data (Jia et al., 2022c), as it maintains improved accuracy than other existing climatological datasets based on comprehensive site validation and product inter-comparison.

2.1.6 VIIRS clear-sky surface albedo

VIIRS blue-sky LSA retrievals were used to filter for albedo dynamic corrections at a 1 km scale. A direct estimation algorithm was developed to retrieve instantaneous blue-sky LSA from clear-sky VIIRS top of the atmosphere (TOA) observations (Wang et al., 2013; Wang et al., 2017), and is currently being produced as an important subset of the VIIRS surface Environmental Data Record (EDR) (Peng et al., 2022; Schueler et al., 2002; Yu, 2022). The direct estimation algorithm employs seven VIIRS bands (M1, M4, M5, M7, M8, M10, and M11) as the major inputs. Further, VIIRS LSA retrievals have been comprehensively validated using global field measurements and albedo reference maps derived from Landsat (Zhou et al., 2016). Officially released VIIRS blue-sky LSA began in 2019; whereas the clear-sky VIIRS LSA in 2013 was produced offline for algorithm testing and improvement. Here, VIIRS LSA was selected as it is the only LSA product that directly provides blue-sky albedo, and the present study aimed to improve its product quality by estimating LSA under clouds.

2.1.7 GLASS all-sky surface albedo

The GLASS gap-free 1 km LSA product is the traditional representative of recovery methodologies, and was employed here for LSA accuracy comparison under clouds. GLASS LSA was retrieved via two direct estimation algorithms from either surface or TOA reflectance (Liang et al., 2021; Liu et al., 2013b). With the help of albedo climatology, a temporal filtering-based method was employed to fuse two albedo results, and the cloudy pixels were filled (Liu et al., 2013a). GLASS BSA and WSA were converted to blue-sky LSA, and linearly interpolated to daily values during pre-processing. Additionally, cloudy-sky GLASS was assessed in 2013 by ground measurements using the same cloudy day mark as VIIRS results. Based on globally distributed 53 Fluxnet sites, the GLASS albedo has an RMSE of 0.059 for all available samples and an RMSE of 0.126 for snow samples. Compared to with MCD43A3, the overall RMSE of clear-sky GLASS albedo was improved to 0.031 (0.080 for snow cases) (Liu et al., 2013b). GLASS albedo products have been widely utilized in scientific research (He et al., 2013; Hu et al., 2016; Li et al., 2021) and considered as one of the essential albedo products for reference (Tao et al., 2014). Characteristics of all satellite products utilized in the study are summarized in Table 1.

Table 1 Characteristics of the satellite products used in the present study.

Product	Spatial resolution	Temporal resolution	Time span used	Usage	Reference
MCD43C3	0.05°	daily	2013, 2015–2019	response variable in snow albedo model training	Schaaf et al. (2020)
MOD08 AOD	1°	monthly	2013, 2015–2019	blue-sky LSA calculation	Platnick et al. (2015)
BTs at 19, 37, and 91 GHz	~ 0.05°	daily	2013, 2015–2019	features in snow albedo model	Brodzik et al. (2018)
All-sky hourly LST	0.045°	hourly	2013, 2015–2019	feature in snow albedo model	Jia et al. (2022b)

All-sky snow mask	1 km	daily	2013, 2015–2019	mark snow and snow-free samples	Helfrich et al. (2007)
Snow-free albedo climatology	1 km	daily	-	prior knowledge	Jia et al. (2022c)
VIIRS LSA	1 km	daily	2013	clear-sky LSA to be filled	Wang et al. (2017)
GLASS LSA	1 km	8-day	2013	dataset for accuracy comparison	Liu et al. (2011)

2.1.8 *In situ* data

To demonstrate the estimation accuracy of VIIRS cloudy-sky LSA, as well as to assess its capacity compared to other gap-free albedo products, ground measurements are essential in this study. SURFRAD is a surface radiation network constructed in 1993 and designed to deliver accurate, continuous, and long-term surface radiation measurements over the CONUS (Augustine et al., 2000), and it has been extensively employed in satellite radiation product validation (Franch et al., 2014; Jia et al., 2018; Wang et al., 2021). Alternatively, Core AmeriFlux sites provide continuous radiation ground measurements, ensure high-quality data collection, and represent a broad range of ecosystems and locations across the CONUS (AmeriFlux, 2021). In total, there are 10 sites in 2013 that recorded surface upward shortwave radiation, and downward shortwave radiation; thus, both were utilized from these networks for albedo computation here. The raw observations marked as “high quality” were averaged within the 1-hour time window centralized by the VIIRS passing time. The time window size doesn’t affect the overall assessment due to the litte albedo variation at hourly scales [generally less than 0.01 based on Wang et al. (2015)]. SURFRAD have 1-min time resolution, thus the high-quality records were averaged once the amount in the window is more than 30. AmeriFlux has 30-min time resolution recorded. As long as they have high-quality records in the time window, these records will be averaged. Site locations are illustrated in Fig. 1, and the data details are listed in Table 2. Ultimately, the 1 km LSA samples were validated in 2013.

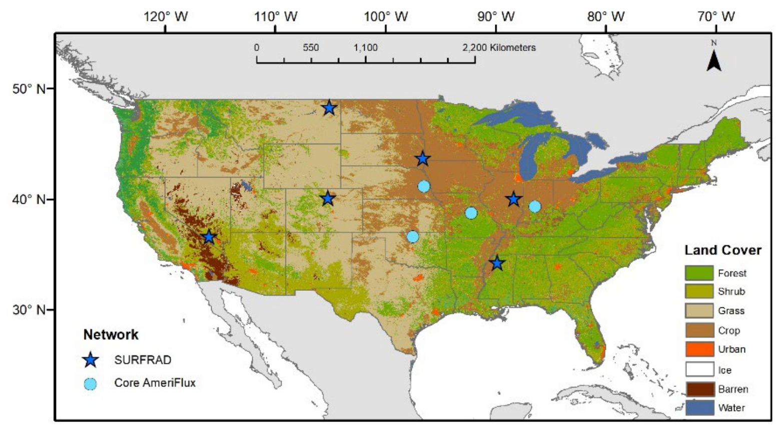

Figure 1. Distribution of sites with land cover types over the continental US (CONUS).

Table 2 Metadata of the *in situ* sites.

Name	Lat. (°)	Long. (°)	Elev. (m)	Land cover
BND	40.0519	-88.3731	230	crop
FPK	48.3078	-105.1017	634	grass
GWN	34.2547	-89.8729	98	pasture
DRA	36.6237	-116.0195	1007	arid shrub
SXF	43.7340	-96.6233	473	grass
TBL	40.1250	-105.2368	1689	grass and shrub
ARM	36.6058	-97.4888	314	crop
MMS	39.3232	-86.4131	275	forest
MOz	38.7441	-92.2000	219	forest
Ne1	41.1651	-96.4766	361	crop

2.2 Methods

2.2.1 Flowchart

A three-step framework was developed for estimating 1 km cloudy-sky LSA (Fig. 2). First, a statistical model was proposed to retrieve all-sky snow LSA from PMW BTs (see Section 2.2.2). MCD43C3 provided clear-sky snow albedo samples from 2015 to 2019 over the CONUS, and the snow albedo was selected according to the IMS snow mask. PMW BTs and all-sky LSTs were considered as input features. The statistical model was trained using the 2015–2019 clear-sky snow samples, and applied to 2013 data for estimating all-sky snow albedo from PMW BTs and LST. It was assumed here that the relationship built by clear-sky samples can be used for all-sky cases.

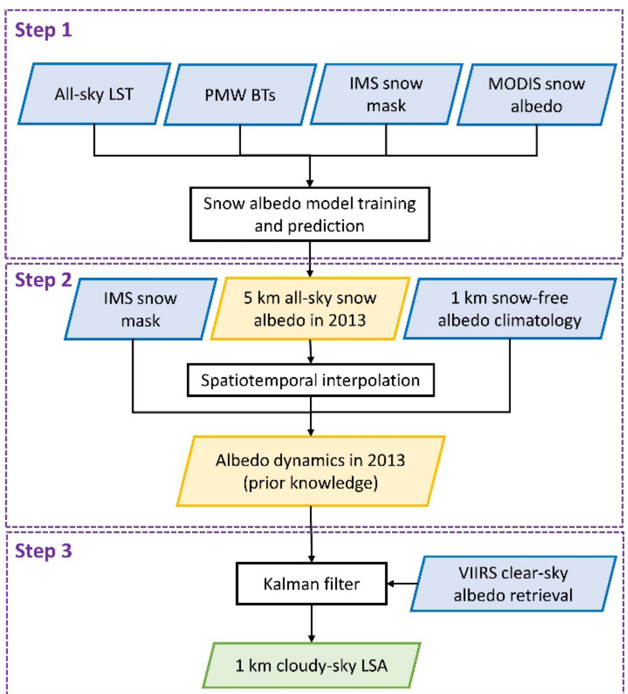

Figure 2. Flowchart of the three-step framework for 1 km cloudy-sky LSA estimation.

Second, prior knowledge of continuous albedo time series was generated by combining snow albedo retrievals and snow-free albedo climatological data. Snow LSA from PMW was bilinearly interpolated to 1 km, and taken as the initial estimate of snow albedo for 2013. Initial downscaling was conducted via bilinear interpolation (snow albedo was further corrected in the third step). Snow-free climatological values were replaced by the PMW albedo on days marked by the IMS snow mask. The combined prior knowledge included the information from both general albedo variation caused by vegetation phenology, as well as real snow variation observed by PMW; thereby making it the first such scheme to estimate LSA that includes both physical constraints and observed disturbances under clouds.

Third, a three-dimensional (geographic location + time) Kalman Filter (KF) was implemented to assimilate the clear-sky VIIRS clear-sky albedo to the albedo dynamic model (Section 2.2.3), as three dimensions can include the maximum level of information from neighboring clear-sky retrievals for each invalid pixel. During the filtering process, the prior knowledge was corrected by available clear-sky VIIRS albedo; thus, the initial estimate of albedo values for invalid pixels was updated to actual albedo under clouds.

2.2.2 Snow albedo estimation from PMW

To capture the LSA variation caused by actual snow falling and melting under clouds, a linear model was proposed to estimate snow albedo from PMW (Eq. (1)):

$$\alpha_{snow} = b_1 T_{91H} + b_2 T_{91V} + b_3 T_{37V} + b_4 T_{19V}$$

$$+ b_5 (T_{91H} - T_{91V}) + b_6 (T_{37H} - T_{37V}) + b_7 (T_{37V} - T_{91V}) + b_8 (T_{19V} - T_{19H}) + b_9 T_s + b_{10}, \quad (1)$$

where α_{snow} is snow albedo, T_{nH} (T_{nV}) is the PMW BT at channel n in H (V) polarization, T_s is the all-sky LST, and b_i is the regression coefficient. The selection of channels and channel differences was based on previous related studies (see the summary in Table 1 of Xiao et al. (2021b)). α_{snow} was identified according to the all-sky IMS snow mask, and in instances of misclassified pixels, α_{snow} values less than corresponding snow-free albedo climatology was excluded. The input features have the same gridding format and very similar resolution with MCD43C3, and they were bilinearly interpolated to match with MCD43C3 pixels, and then input features were extracted based on dates and locations of the selected MCD43C3 samples. It should be noted that the issue of spatial mismatch and the simple bilinear interpolation are the potential source of errors in albedo estimation. An improved representation of footprint mismatch and albedo spatial heterogeneity should be explored in the future study.

The relationships between PMW observations and snow are substantially influenced by topography (i.e., elevation, slope, and aspect). Whereas previous studies have typically considered topographic factors as independent variables, complicated terrains still create considerable uncertainty in estimates (Dai et al., 2017; Liu et al., 2018; Xiao et al., 2021a). To minimize this impact, a pixel-wise modeling was employed by only using time series information from clear days at each pixel (Jia et al., 2021; Sun et al., 2019). As the topography was constant over time, its impacts could be ignored. Further, if snow events are rare in some regions at lower or mid-latitudes, the model searched neighboring pixels (< 100 km) to acquire enough samples for model regression.

A sensitivity analysis was performed in advance to demonstrate the importance of all input data for snow albedo estimates from PMW observations. Following training the snow albedo model with samples from 2015 to 2019, random noises of certain levels were added to an input feature to increase its relative errors during the 2013 prediction, while maintaining all other input data (control variates). Here, the level of noise corresponded to specific percentages of the feature values. As the percentages were adjusted, the noise magnitude of the feature to be examined also changed, and the final estimates of RMSE of snow albedo changed accordingly. To improve computational speed, samples were randomly selected at 50 locations according to different plant functional types (FPTs) over the CONUS.

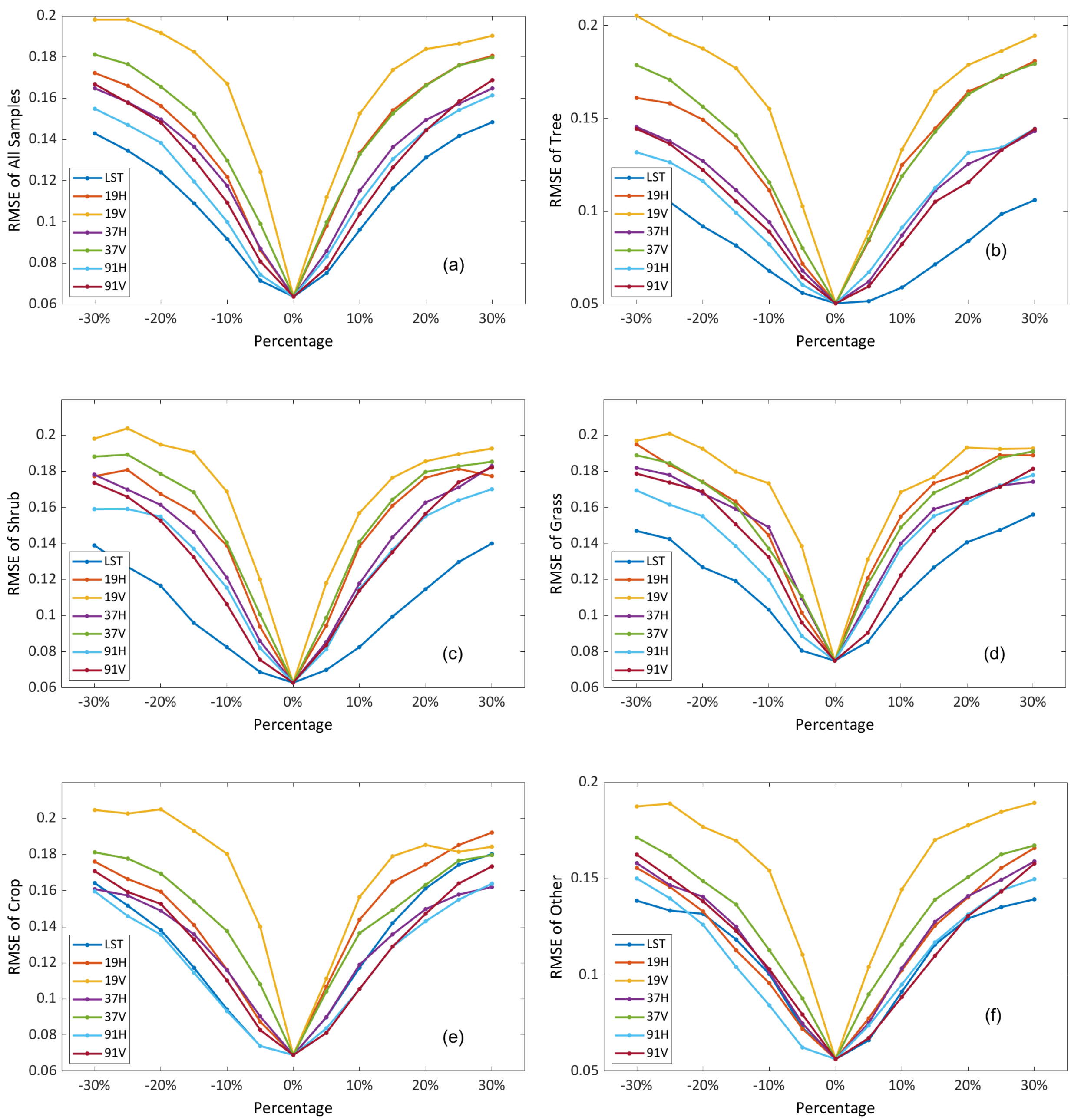

Figure 3. RMSE variation of passive microwave (PMW)-derived snow albedo by introducing error to all input data, for different plant functional types (PFTs): (a) all samples, (b) tree, (c) shrub, (d) grass, (e) crop, and (f) other types.

19V was the most important input band of the statistical models across all PFTs (Fig. 3). Notably, lower frequencies have improved correlations with snow/ice, as confirmed by previous estimates of sea ice albedo using PMW observations (Laine et al., 2011). 37V was the second most important factor for most types (except croplands, where 19H was equally important). In comparison, snow albedo had the lowest sensitivity towards all-sky LST, especially for forest regions. This is mainly because the underlying surface of forest regions is dominated by canopy cover, and LST is more closely correlated to air temperature rather than soil temperature. Based on Jia et al. (2022b), the RMSEs of cloudy-sky LST vary from 1.5 K to 5 K through validation at 200 sites over the globe. The LSTs of snow-covered surface is assumed to be within 200 K – 273 K, and the relative uncertainty of LST is 1% to 4% that will not introduce substantial errors to albedo estimation. No further techniques for band selection were employed here, as all input data had a clear impact on the model prediction.

2.2.3 Spatiotemporal filtering

KF is a basic data fusion method for assimilating discontinuous observations into a dynamic model (Welch and Bishop, 1995). Here, the dynamic model took the form of prior knowledge. Once a new observation was made available, the model prediction was updated using a weighted average of the available observations and initial modeling result. As the model iteratively predicts from the revised values, the prediction of future cloudy days will be recovered with higher accuracy; however, basic KF is typically utilized along the temporal dimension, and thus only a limited number of clear-sky observations can be assimilated. Therefore, a spatial module was added, and a 3D-KF method was created in previous studies to assimilate spatiotemporally adjacent clear-sky retrievals within a spatial window (Jia et al., 2022a; Zhang et al., 2013). This process included two independent modules: In the temporal module, the dynamical albedo series from prior knowledge at window center *c* was represented by an albedo dynamic model (Eq. (2)):

$$\widehat{\alpha_{c,d}^{t}}^{-} = \widehat{\alpha_{c,d-1}^{t}} + F_{c,d}^{t}, \tag{2}$$

$$\widehat{\alpha_{c,d}^{t}} = \widehat{\alpha_{c,d}^{t}}^{-} + K_{d}^{t}(\alpha_{d,c} - \widehat{\alpha_{c,d}^{t}}^{-}), \tag{3}$$

$$K_{d}^{t} = P^{-}{}_{t,d}(P^{-}{}_{t,d} + R)^{-1}, \tag{4}$$

$$P_{t,d} = (I - K_{k}^{t})P^{-}{}_{t,d}, \tag{5}$$

where $\widehat{\alpha_{c,d}^{t}}^{-}$ is the initial albedo prediction of the dynamic model on day *d* from *d*-1, $F_{c,d}^{t}$ is the albedo difference between two days based on prior knowledge, while the – symbol means it is the initial model prediction. To minimize the influence of systematic biases from prior knowledge, only the albedo differences of neighboring days were used for building the dynamic model (rather than the absolute albedo values).

If a valid VIIRS LSA retrieval ($\alpha_{d,c}$) is available on *d* at *c*, $\widehat{\alpha_{c,d}^{t}}^{-}$ will be corrected to $\widehat{\alpha_{c,d}^{t}}$ by Kalman Gain K_{d}^{t} (Eq. (3)). K_{d}^{t} was then determined by prediction error $P^{-}{}_{t,d}$ of the temporal module and VIIRS retrieval error *R* according to Eq. (4). *R* is constant and set to 0.04 based on Zhou et al. (2016); whereas the initial uncertainty magnitude of the model prediction was set to the same as the modeled error of PMW albedo compared with MCD43C3 in 2013. Prediction uncertainty was also corrected to $P_{t,d}$ (Eq. (5)), where I is a unit matrix. The KF is iterative and the predicted albedo on d+1 was based on $\widehat{\alpha_{c,d}^{t}}$ (Eq. (2)).

If no valid VIIRS LSA were present at c on d, the temporal module can still predict $\widehat{\alpha_{c,d}^{t}}^{-}$, while the spatial module was activated to identify spatially adjacent clear-sky VIIRS LSA pixels within a spatial window as references for correction. When the spatial module was activated, any adjacently available VIIRS LSA ($\alpha_{d,m}$) at the adjacent pixel m will firstly correct corresponding prior knowledge ($\widehat{\alpha_{m,d}^{s}}^{-}$) according to Eq. (6):

$$\widehat{\alpha_{m,d}^{s}} = \widehat{\alpha_{m,d}^{s}}^{-} + K_d^s(\alpha_{d,m} - \widehat{\alpha_{m,d}^{t}}^{-}), \tag{6}$$

where K_d^s is the Kalman gain of the spatial module, and the remaining calculation is similar to Eq. (4). Then, the spatial module predicts the possible center albedo values ($\widehat{\alpha_{c,d}^{s}}^{-}$) from all corrected values at adjacent locations (the total number of m is N), and are averaged to obtain the output of the spatial module ($\widehat{\alpha_{c,d}^{s}}^{-}$). In Eq. (7), $F_{c,d}^{s}$ is the albedo difference of c and m on day d (based on prior knowledge data), and the weight w_m is pre-determined by the relative magnitude of the correlation coefficient (R) of prior knowledge series between c and m:

$$\widehat{\alpha_{c,d}^{s}}^{-} = \frac{\sum_1^N w_m(\widehat{\alpha_{m,d}^{d}} + F_{c,d}^{s})}{N}. \tag{7}$$

Pixel m with R values < 0.8 were excluded, as higher R values imply that m has a similar albedo response as the target c towards vegetation phenology and snow cover. The spatial module typically produced an accurate prediction to c, as it only processed one-time predictions from neighboring clear-sky pixels; thus, its uncertainty ($P^{-}{}_{s,d}$) was set to 0.05, slightly larger than clear-sky retrieval. Finally, by averaging $\widehat{\alpha_{c,d}^{s}}^{-}$ from the spatial module, and $\widehat{\alpha_{c,d}^{t}}^{-}$ from the temporal module, the 1 km LSA under clouds ($\widehat{\alpha_{c,d}}$) was estimated via (Eq. (8)):

$$\widehat{\alpha_{c,d}} = \frac{P^{-}{}_{t,d}}{P^{-}{}_{t,d}+P^{-}{}_{s,d}} \widehat{\alpha^{s}_{c,d}}^{-} + \frac{P^{-}{}_{s,d}}{P^{-}{}_{t,d}+P^{-}{}_{s,d}} \widehat{\alpha^{t}_{c,d}}^{-}, \quad (8)$$

where weights of $\widehat{\alpha^{s}_{c,d}}^{-}$ and $\widehat{\alpha^{t}_{c,d}}^{-}$ are determined by the relative magnitude of the prediction errors of spatial ($P^{-}{}_{s,d}$) and temporal ($P^{-}{}_{t,d}$) modules. To improve computational efficiency, two modules were designed independently. Specifically, if VIIRS LSA was available on *d* at *c*, only the correction function of the temporal module (Eqs. 3–5) was activated; otherwise, the cloudy-sky LSA was predicted from both modules. Additionally, the spatial window was set to 100 km in order to balance the number of VIIRS LSA pixels available with computational resources; whereas the adjacent pixel number inside the window was reduced based on *R*.

3 Results and discussion

3.1 Assessment of PMW-derived snow albedo

The statistical model of snow albedo was evaluated for 2013 over the CONUS, and the prediction results were compared with corresponding high-quality MCD43C3 snow samples masked by IMS. Samples were extracted and paired across basic PFTs (tree, shrub, grass, and crop, classified by MCD12C1), and each type was randomly sampled at 500 locations. Comparative results are illustrated in Fig. 4.

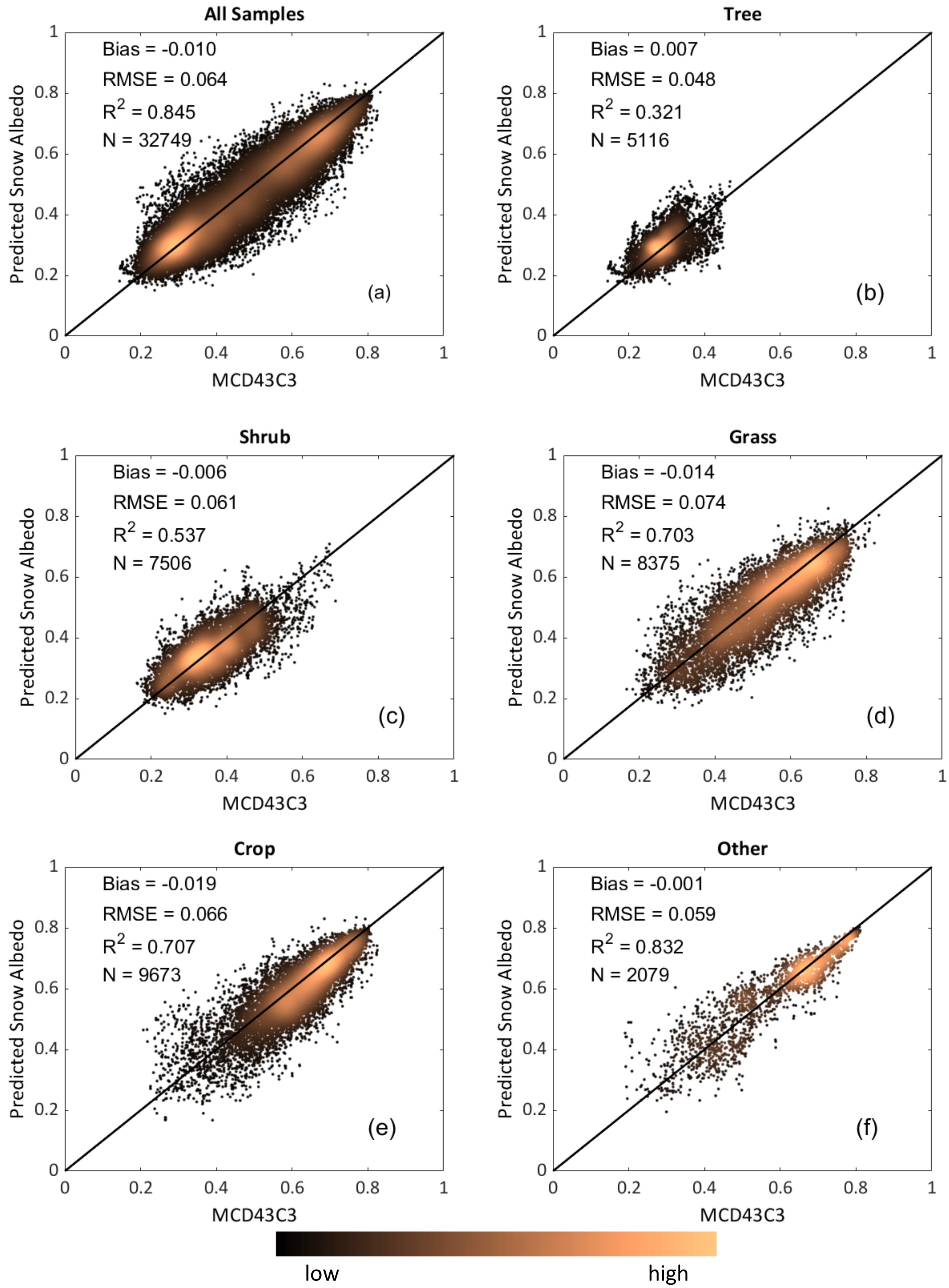

Figure 4. Density scatterplots of predicted snow albedo and corresponding MCD43C3 for different plant functional types (PFTs): (a) all selected samples, (b) trees, (c) shrubs, (d) grasses, (d) crops, and (e) other.

Based on the 2013 validation, the overall RMSE of the PMW-derived snow albedo was 0.064, with a bias of -0.010 and R^2 of 0.845. In addition, RMSEs didn't change considerably at different PFTs and biases remain low. Some samples with small albedo values could have been misclassified by the IMS snow mask, although these samples still fell along the 1:1 line, suggesting that this framework was tolerant of snow misclassification. In comparison, forest and shrub samples (Figs. 4b and c) had lower R^2 of 0.321 and 0.537, respectively. This is because they displayed a small snow albedo value range more related to vegetation height; thus, snowfall and melting do not considerably affect the reflective surface landscape. Nevertheless, forest and shrub samples still matched closely with the 1:1 line, with few biases. Further, grass and crops produced higher R^2 of 0.703 and 0.707, respectively, with a large snow albedo range (Figs. 4d and e). Crop samples were relatively scattered across the lower snow albedo range, and Fig. 4f displayed a similar scatter pattern due to the relatively limited available training samples in lower value ranges. These scattered samples can be also partially attributed to snow aging as PMW data is not sensitive to the snow color darkening that affects spectral albedo at visible bands. Therefore, PMW-estimated results may have positive bias for dark snow samples at low snow albedo range (Figs. 4e). Nevertheless, surface characteristics (e.g., LST) are also impacted during snow aging, providing an auxiliary information for snow albedo estimation. Overall, the samples still match 1:1 line with RMSE less than 0.07. The slow albedo variation due to snow aging will be further corrected by clear-sky retrievals in step three. The accuracies of all snow pixels over the CONUS were further predicted to generate the corresponding distribution maps (Fig. 5). To ensure the representativeness of the statistics, only pixels with snow days > 5 in 2013 were included in the maps.

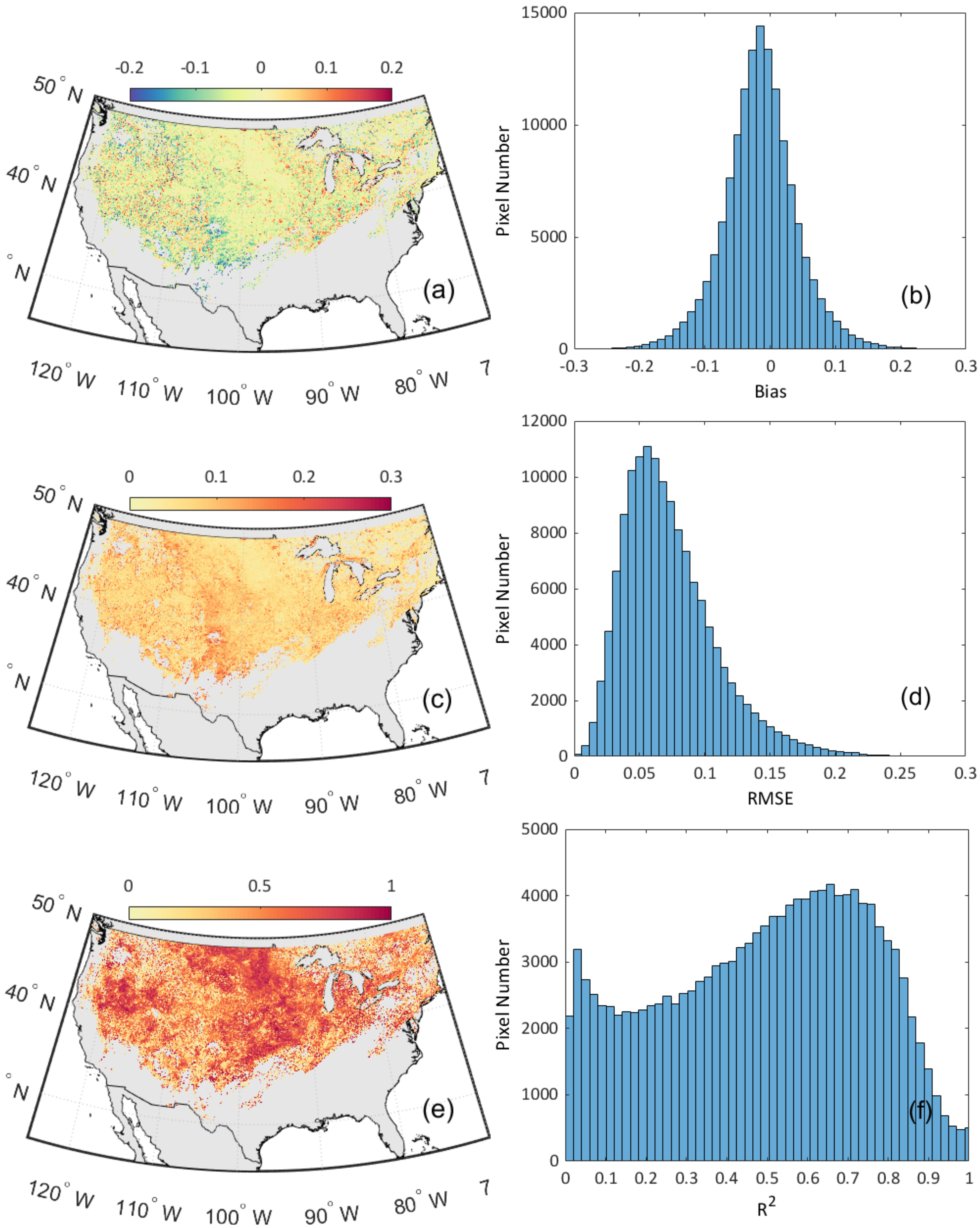

Figure 5. Accuracy patterns and corresponding histograms over the CONUS: (a, b) bias, (c, d) RMSE, and (e, f) R^2.

The accuracy patterns in Fig. 5 indicate that the predicted results over the CONUS were relatively consistent, as ~90% of pixels produced a bias within ±0.100 (median value, -0.011; Fig. 5b), and no clear spatial patterns of large error emerged. Comparatively, the west did produce more scattered, larger-biased pixels than the east (Fig. 5a), likely related to its more complex topography and elevation producing greater uncertainties during pixel matching of input features. Further, the southcentral region was characterized by a slightly negative bias pattern, and it was inferred here that was attributable to the limited snow sampling history. The RMSE suggested that 95% of the pixels produced values < 0.200 (median, 0.07; Fig. 5d). The central region produced a relatively higher RMSE, likely because it is dominated by grass and croplands (Fig. 5c) with higher snow albedo values (translating into slightly higher RMSE values; Fig. 4). The distribution of R^2 was not clustered (maximum = 0.66, Fig. 5f), and was primarily affected by forest and shrubs. The proposed model well estimated the overall magnitude of snow albedo for trees and shrubs (Figs. 4b and c). However, as albedo variation at these regions is less sensitive to the snow cover compared to other land cover types, capturing the all-sky snow albedo variation with high confidence (R^2) at tree and shrub covered regions remains a challenge.

Accordingly, it was concluded here (Fig. 5) that the proposed scheme can be used on continental scales.

Feb. 14, 2013 Dec. 05, 2013

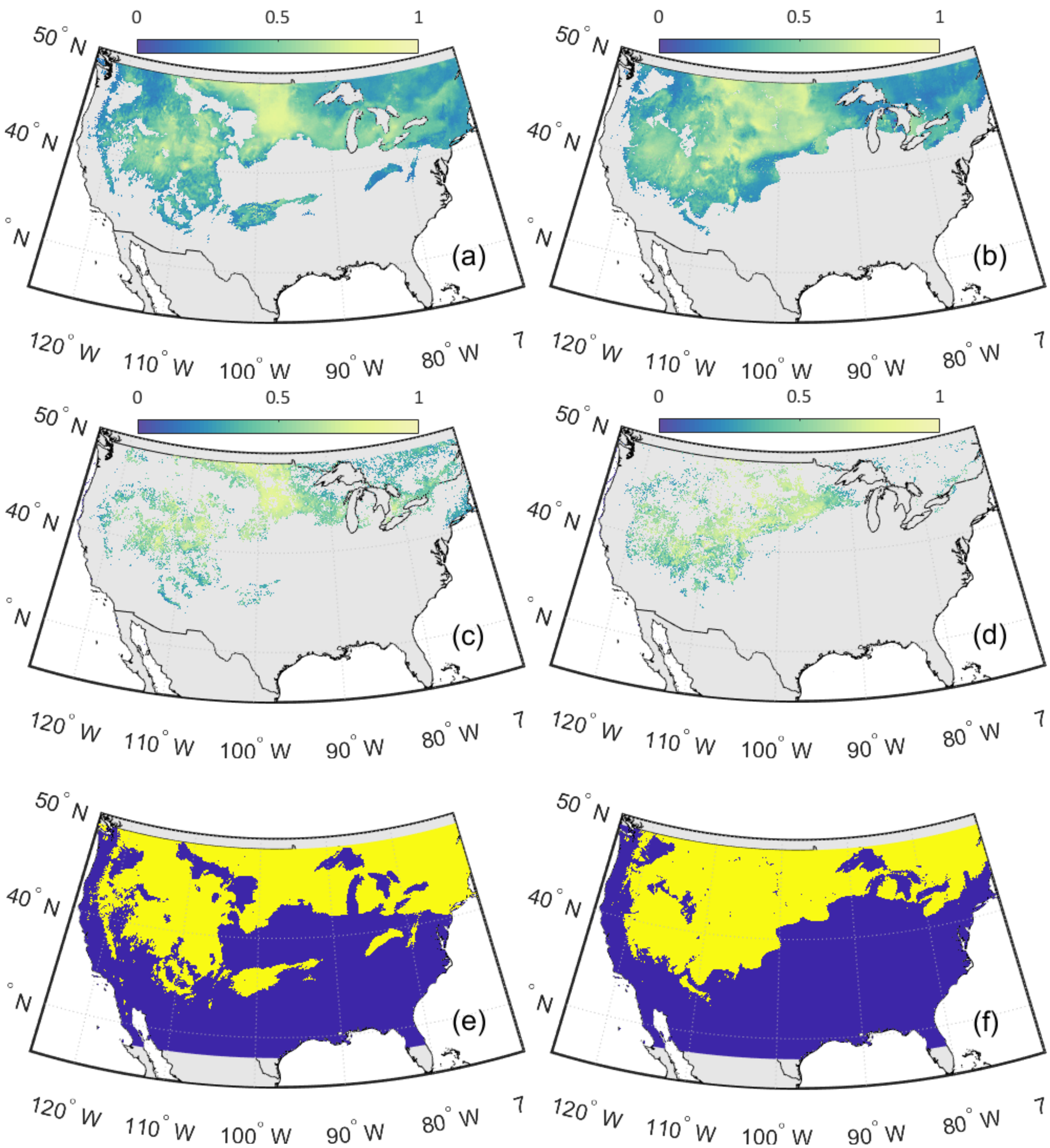

Figure 6. Snow albedo on (a, c, e) Feb. 14 and (b, d, f) Dec. 05 in 2013 for (a, b) PMW-derived results, (b, d) MCD43C3, and (e, f) IMS snow mask, where snow pixels are marked in yellow.

The snow albedo maps on Feb. 14 and Dec. 5, two randomly selected dates from 2013, are drawn in Fig. 6, where the corresponding MCD43C3 and IMS snow mask are also included. The

PMW-derived snow albedo maps did well to recover the invalid pixels compared with MCD43C3 and the corresponding snow mask. Figure 6a and b illustrate that the recovered snow albedo maps on different days produced relatively continuous and reasonable spatial patterns, with natural transitions from high to low value regions. Further, they matched well with clear-sky pixels in Fig. 6c and d. The limited number of clear-sky pixel patterns here also indicates the difficulty when accurately reconstructing all cloudy-sky pixels based solely on interpolation.

3.2 Validation of 1 km cloudy-sky LSA

After combining the PMW-derived snow albedo and snow-free albedo climatological data, the albedo dynamic series and further filtered clear-sky VIIRS albedo was generated to obtain the 1 km cloudy-sky LSA, which in turn was validated using 10 ground sites from SURFRAD and Core AmeriFlux networks. GLASS LSA samples were also extracted and validated for accuracy comparison (Fig. 7); whereas corresponding shortwave net radiation (RSN) was incorporated to demonstrate the impact of LSA error on SEB, and downward shortwave radiation was directly from ground measurements.

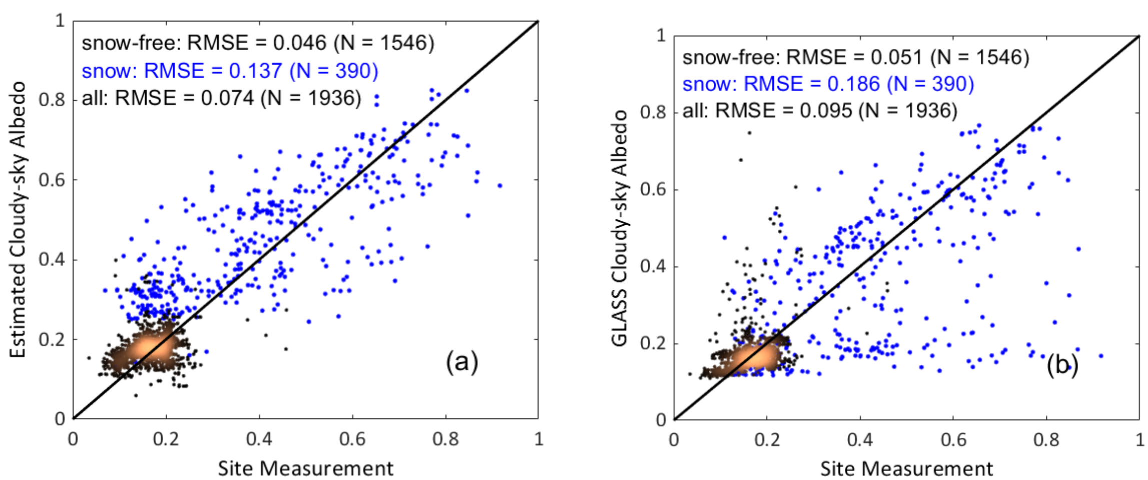

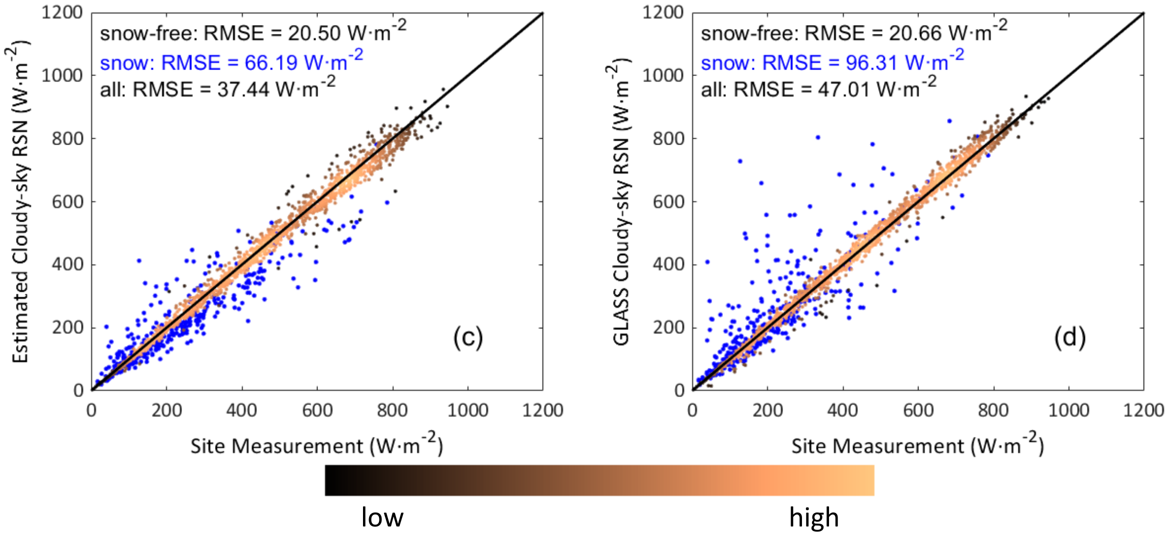

Figure 7. Density scatterplots of: (a, b) cloudy-sky albedo, and (c, d) corresponding shortwave net radiation (RSN) samples from (a, c) this study, and (b, d) GLASS.

The estimated cloudy-sky LSA in the present study produced better accuracy and scatter patterns than GLASS, especially over snow cover. The overall RMSE of the present study was 0.074 (bias, 0.017; R^2, 0.75), compared to that of GLASS being 0.095 (bias, -0.012; R^2, 0.54). Comparatively, the RMSE for snow cases in this study (0.137) was more accurate than that for GLASS (0.186). Furthermore, GLASS produced numerous scattered samples with considerable variations from in situ measurements, partly due to cloudy-sky GLASS albedo values missing snow cases without actual observations included in the algorithm (Liu et al., 2013a). After calculating the corresponding RSN using the noon downward shortwave radiation of site observations, it was found that the RSN of this study matched with the 1:1 line well, while the RMSE of snow cases (66.19 W·m^{-2}) was more accurate than the corresponding GLASS samples (96.31 W·m^{-2}). Although the majority of GLASS samples have higher accuracy, suggesting that the albedo climatology-based method is sufficient for predicting LSA under clouds for snow-free cases, GLASS RSN produces some anomalies that substantially affect accuracy, primarily with cloudy-sky snow cases. The comparison in Fig. 7 supports that cloudy-sky snow cases can caused considerable abnormalities in the traditional pixel reconstruction methods; whereas the method proposed by the present study addressed this issue by including actual signals under clouds.

The RMSE statistics at each site are also listed in Table 3. The snow median value of the present study was 0.144 (values ranging 0.124–0.171); whereas GLASS snow cases produced a median RMSE of 0.185 (0.061–0.278). Notably, both produced close RMSEs for snow-free cases, although the filtering methods were different. The GWN and DRA sites are snow-free, so they were recovered using strictly climatological data as prior knowledge. GLASS produced higher snow albedo accuracies at MMS and MOz than the present study possibly due to the higher spatial heterogeneity at these two AmeriFlux forest sites and GLASS only utilized temporal filtering. After removing these two sites, two groups of snow albedo RMSE statistics (Table 3) have significant difference (p-value = 0.027) based on the single factor analysis of variance.

Table 3. Cloudy-sky LSA RMSE statistics of individual sites.

Site	**This study (snow)**	**This study (snow-free)**	**GLASS (snow)**	**GLASS (snow-free)**
BND	0.133	0.062	0.278	0.088
FPK	0.124	0.021	0.118	0.039
GWN	-	0.031	-	0.046
DRA	-	0.030	-	0.029
SXF	0.076	0.045	0.142	0.063
TBL	0.161	0.047	0.229	0.053
ARM	0.171	0.044	0.273	0.030
MMS	0.149	0.050	0.061	0.021
MOz	0.142	0.047	0.061	0.017

Ne1	0.145	0.044	0.262	0.066
Median	0.144	0.045	0.185	0.043

To demonstrate the present model's capacity to capture ephemeral snow coverage, temporal analyses were performed across distinct snow events from four sites. The cloudy-sky LSA of the present study was combined with VIIRS clear-sky retrievals, and depicted as all-sky LSA series in Fig. 8. Compared with ground measurements, the data in Fig. 8 illustrates that the all-sky series of present study can capture short-term snow events, closely matching with the in situ data, even though some snow durations were completely covered by clouds. In comparison, the GLASS series can only reconstruct snow albedo where there is an obvious snow season (Fig. 8b). Even for longer duration snow cases (DOY 350; Fig 8a, c, and d), GLASS may miss peak values and dates, due to its limited capture of overall snow albedo variation.

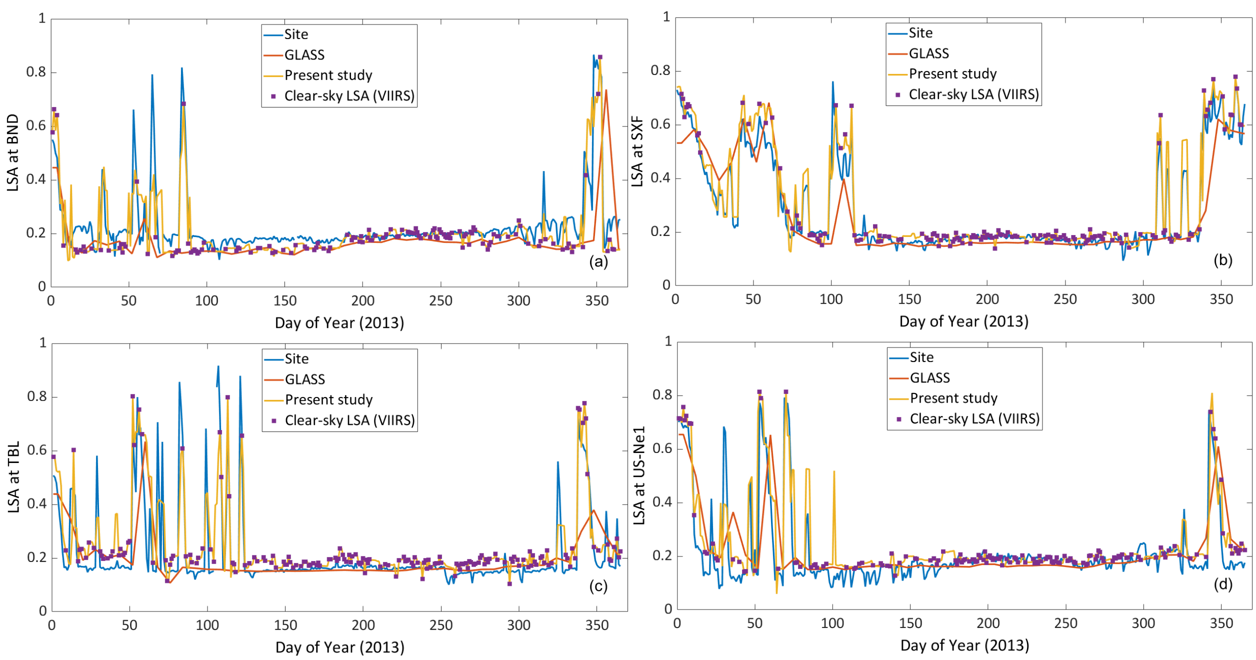

Figure 8. Temporal variation of LSA at four sites: (a) BND, (b) SXF, (c) TBL, and (d) Ne1.

Furthermore, the proposed framework was implemented at the regional scale to test the spatial continuity of 1 km images. The tile H11V04 (located over the Great Lakes, and the same tile number for MODIS) was chosen for its clear snow patterns. Three days (Jan. 17, 19, and 21, 2013) were selected, as they encompassed a short snow coverage event (circled in Fig 9a) for a detailed analysis. The all-sky LSA maps were compared with corresponding gap-free GLASS LSA maps, and the results are presented in Fig. 9.

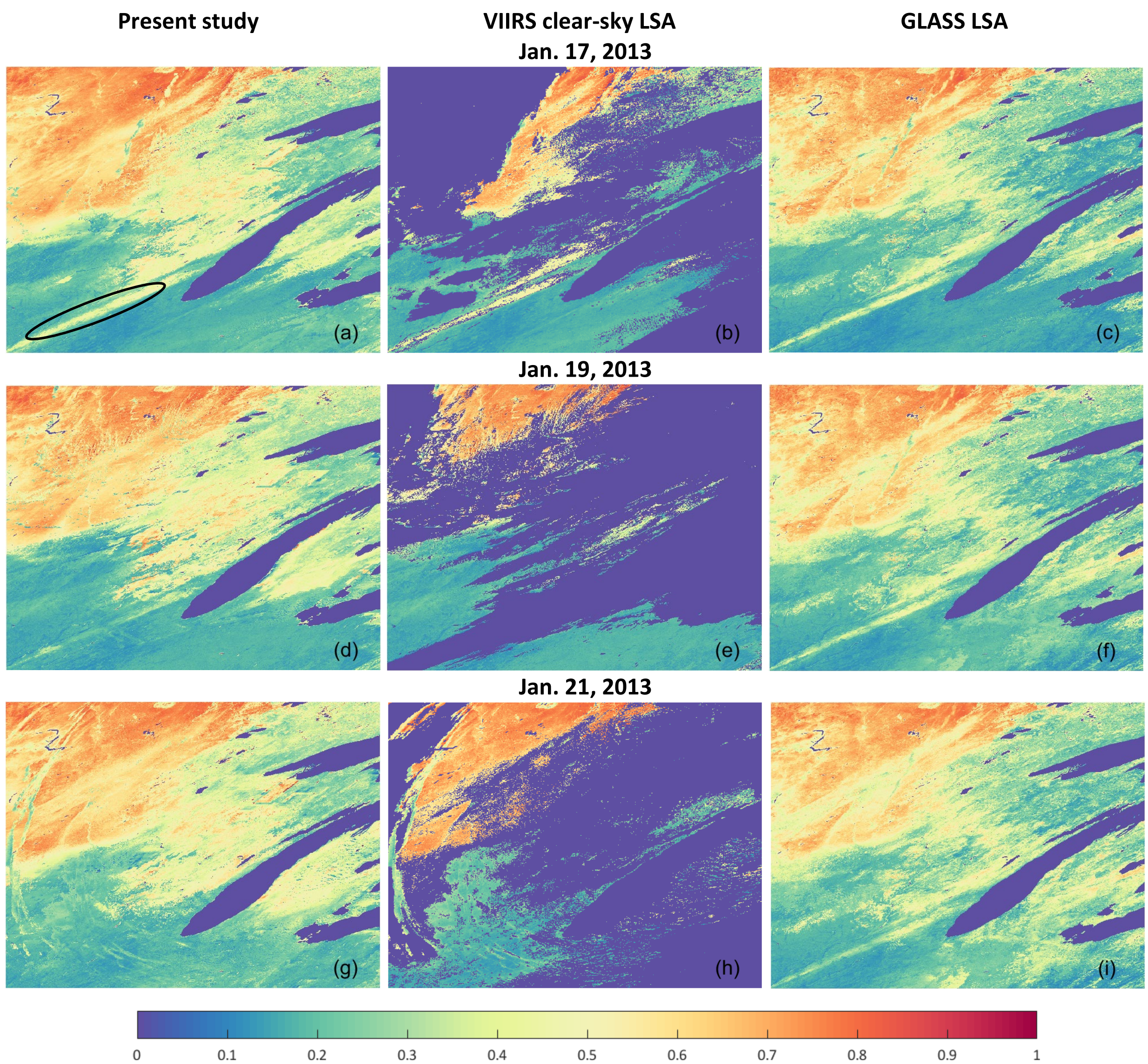

Figure 9. LSA maps of H11V04 on (a–c) Jan. 17, (d–e) Jan. 19, and (f–i) Jan. 21, 2013, from (a, d, g) all-sky LSA, (b, e, h) VIIRS clear-sky LSA, and (c, f, i) GLASS. Water and cloudy pixels are masked as invalid by dark blue color.

The recovered cloudy-sky LSA (Fig. 9a, d, and g) produced good spatial continuity with clear-sky VIIRS pixels (Fig. 9b, e, and h), and reflects clear spatial details. There is long-term snow coverage with high surface albedo values are located to the top of the image, while snow-free albedo is concentrated towards the bottom. The overall spatial patterns closely matched with GLASS LSA maps (Fig. 9c, f, and i) without artificial textures; however, GLASS displayed limited spatial pattern changes over these three days, whereas the all-sky albedo of the present study illustrated some important detailed variation. For example, the circled short-term snow albedo event at the bottom left of the image was taken as an example. Here, this short-term snow coverage was observed by VIIRS on Jan. 17 (Fig. 9a and b), and is also shown on the corresponding GLASS map (Fig. 9c). It had almost melted on Jan. 19, as evidenced by the recovered cloudy-sky LSA from the present study (Fig. 9d), while complete melting was observed by Jan. 21 according to the VIIRS clear-sky retrievals (Fig. 9h), and the recovered all-sky LSA from the present study reflected this ephemeral snow events correctly (Fig. 9g); however, this snow coverage event persists on all GLASS maps for these days (Figs. 9c, f, and i). Such comparisons indicate that the proposed methodology can successfully recover cloudy-sky LSA with spatial continuity and texture details, especially for disturbances caused by snow.

4 Conclusions

LSA characterizes the ability of the Earth's surface to reflect solar radiation, and plays a central role in the SEB. A novel three-step framework for recovering cloudy-sky LSA was thus proposed here: 1) All-sky snow albedo was estimated from PMW observations based on a statistical model; 2) Albedo dynamics were initially generated by combining the all-sky snow albedo with snow-free albedo climatological data; and, 3) The 1 km cloudy-sky LSA was estimated after assimilating 1 km VIIRS clear-sky retrievals to the albedo dynamic series.

The all-sky snow albedo was estimated from PMW BTs over the CONUS for 2013. Based on comparisons with high-quality MODIS clear-sky pixels, the overall RMSE was 0.064 (bias, -0.010; R^2, 0.845), and the accuracy kept stable across different PFTs. In addition, when compared with MCD43C3 and the corresponding snow mask, the PMW-derived snow albedo adequately recovered invalid pixel data to produce a continuous spatial pattern over the CONUS.

Cloudy-sky albedo was then estimated at the 1 km scale after filtering the VIIRS retrieval using combined snow albedo with snow-free albedo climatological data. Based on 10 ground sites, the overall RMSE of the recovered cloudy-sky LSA was 0.074 (bias, 0.017; R^2, 0.75); whereas the overall RMSE of all-sky GLASS LSA was 0.095 (bias, -0.012; R^2, 0.54). In comparison, the RMSE of 0.137 obtained for snow cases of this study was notably more accurate than GLASS (0.186). The impacts of albedo uncertainty on RSN was further evaluated, and indicated that the RMSE of snow cases of VIIRS cloudy-sky LSA was 66.19 $W \cdot m^{-2}$, more accurate than the corresponding GLASS samples (96.31 $W \cdot m^{-2}$), while the uncertainty due to snow albedo of GLASS further caused a considerable number of abnormal RSN values. The 1 km all-sky LSA displayed satisfactory spatiotemporal continuity, and successfully captured short-term albedo disturbances from snow.

To the best of the author's knowledge, the research here represents the first study to includes PMW in the cloudy-sky LSA recovery for improving the uncertainty caused by seasonal snow albedo. Although it was supplemented here with VIIRS data, the presented approach is sensor independent, and maintains the practicality to be used in other LSA products, such as MODIS and AVHRR. Its downscaling accuracy, however, may be limited by surface heterogeneity due to the relatively coarse resolution of PMW data, but employing active microwave observations could represent a potential solution for improving future framework, particularly in high elevation regions. Besides, this framework is currently not suitable for real-time albedo production due to input latency and computation efficiency. Further, capturing all-sky snow albedo variation in details at tree and shrub regions remains a challenge to be explored in the future. Additionally, the impact of snow darkening, surface snow wetness, snow morphology, and grain size change during snow aging on snow albedo needs to be considered in the future by adding snow melting model. This framework further improves the accuracy of cloudy-sky LSA estimation, enables the capture of more realistic snow impacts on SEB, and can ultimately broaden the application of albedo products for snow modeling, irrigation management, flood forecasting, and other essential processes on which modern humanity is dependent.

Acknowledgments

This study was financially supported by the National Oceanic and Atmospheric Administration (NOAA) grant (NA19NES4320002) through the Cooperative Institute for Climate and Satellite-CICS at the University of Maryland, College Park. The scientific results and conclusions, as well as any views or opinions expressed herein, are those of the authors, and do not necessarily reflect those of NOAA, or the Department of Commerce. The authors would like to thank NASA for providing MODIS albedo and AOD products (https://earthdata.nasa.gov/), as well as the National Snow and Ice Data Center (NSIDC) for providing EASE-Grid 2.0 PMW data (https://nsidc.org/pmesdr/) and IMS snow mark data (https://nsidc.org/data/g02156/), as well as the GLASS team for providing gap-free albedo, snow-free albedo climatology, and all-sky LST products (http://glass.umd.edu/Download.html). We also thank SURFRAD (https://gml.noaa.gov/grad/surfrad/) and AmeriFlux (https://ameriflux.lbl.gov/) networks for providing ground measurement information.

Declaration of Competing Interest

The authors declare no known competing financial interests or personal relationships that could have influenced the work reported in this paper.

Author Contributions

Aolin Jia: Conceptualization, Data curation, Formal analysis, Investigation, Methodology, Software, Validation, Visualization, Writing - original draft, Writing - review & editing. Dongdong Wang: Conceptualization, Funding acquisition, Project Administration, Resources, Supervision, Formal analysis, Investigation, Methodology, Writing review & editing. Shunlin Liang: Funding acquisition, Formal analysis, Writing - review & editing. Jingjing Peng: Project administration, Resources, Formal analysis, Writing review & editing. Yunyue Yu: Funding acquisition, Project administration, Formal analysis, Writing - review & editing.

References

Abdalati, W., & Steffen, K. (1997). Snowmelt on the Greenland ice sheet as derived from passive microwave satellite data. *Journal of Climate, 10*, 165-175

AmeriFlux (2021). What are the AmeriFlux Core Sites? In. https://ameriflux.lbl.gov/sites/ameriflux-core-sites/ (access date: July 30, 2021)

Anderson, R.G., Canadell, J.G., Randerson, J.T., Jackson, R.B., Hungate, B.A., Baldocchi, D.D., Ban-Weiss, G.A., Bonan, G.B., Caldeira, K., & Cao, L. (2011). Biophysical considerations in forestry for climate protection. *Frontiers in Ecology and the Environment, 9*, 174-182

Augustine, J.A., DeLuisi, J.J., & Long, C.N. (2000). SURFRAD - A national surface radiation budget network for atmospheric research. *Bulletin of the American Meteorological Society, 81*, 2341-2357

Bair, E.H., Rittger, K., Skiles, S.M., & Dozier, J. (2019). An examination of snow albedo estimates from MODIS and their impact on snow water equivalent reconstruction. *Water Resources Research, 55*, 7826-7842

Barlage, M., Chen, F., Tewari, M., Ikeda, K., Gochis, D., Dudhia, J., Rasmussen, R., Livneh, B., Ek, M., & Mitchell, K. (2010). Noah land surface model modifications to improve snowpack prediction in the Colorado Rocky Mountains. *Journal of Geophysical Research: Atmospheres, 115*

Boussetta, S., Balsamo, G., Dutra, E., Beljaars, A., & Albergel, C. (2015). Assimilation of surface albedo and vegetation states from satellite observations and their impact on numerical weather prediction. *Remote Sensing of Environment, 163*, 111-126

Brodzik, M., & Long, D. (2018). Calibrated passive microwave daily EASE-grid 2.0 brightness temperature ESDR (CETB): Algorithm theoretical basis document. *MEaSUREs Project White Paper*

Brodzik, M.J., Long, D.G., & Hardman, M.A. (2018). Best practices in crafting the calibrated, enhanced-resolution passive-microwave EASE-Grid 2.0 brightness temperature earth system data record. *Remote Sensing, 10*, 1793

Brown, L.C., Howell, S.E., Mortin, J., & Derksen, C. (2014). Evaluation of the Interactive Multisensor Snow and Ice Mapping System (IMS) for monitoring sea ice phenology. *Remote Sensing of Environment, 147*, 65-78

Bryant, A.C., Painter, T.H., Deems, J.S., & Bender, S.M. (2013). Impact of dust radiative forcing in snow on accuracy of operational runoff prediction in the Upper Colorado River Basin. *Geophysical Research Letters, 40*, 3945-3949

Cao, R., Chen, Y., Shen, M., Chen, J., Zhou, J., Wang, C., & Yang, W. (2018). A simple method to improve the quality of NDVI time-series data by integrating spatiotemporal information with the Savitzky-Golay filter. *Remote Sensing of Environment, 217*, 244-257

Chen, A., Li, W., Li, W., & Liu, X. (2014). An observational study of snow aging and the seasonal variation of snow albedo by using data from Col de Porte, France. *Chinese Science Bulletin, 59*, 4881-4889

Chen, C., Lakhankar, T., Romanov, P., Helfrich, S., Powell, A., & Khanbilvardi, R. (2012). Validation of NOAA-interactive multisensor snow and ice mapping system (IMS) by comparison with ground-based measurements over continental United States. *Remote Sensing, 4*, 1134-1145

Chen, J.M., & Liu, J. (2020). Evolution of evapotranspiration models using thermal and shortwave remote sensing data. *Remote Sensing of Environment, 237*

Chiu, J., Paredes-Mesa, S., Lakhankar, T., Romanov, P., Krakauer, N., Khanbilvardi, R., & Ferraro, R. (2020). Intercomparison and validation of MIRS, MSPPS, and IMS snow cover products. *Advances in Meteorology, 2020*

Cho, D., Bae, D., Yoo, C., Im, J., Lee, Y., & Lee, S. (2022). All-Sky 1 km MODIS Land Surface Temperature Reconstruction Considering Cloud Effects Based on Machine Learning. *Remote Sensing, 14*, 1815

Chu, D., Shen, H., Guan, X., Chen, J.M., Li, X., Li, J., & Zhang, L. (2021). Long time-series NDVI reconstruction in cloud-prone regions via spatio-temporal tensor completion. *Remote Sensing of Environment, 264*, 112632

COMET (2015). *Microwave Remote Sensing: Land and Ocean Surface Applications*. (2nd ed.). The University Corporation for Atmospheric Research

Cui, Y., Long, D., Hong, Y., Zeng, C., Zhou, J., Han, Z., Liu, R., & Wan, W. (2016). Validation and reconstruction of FY-3B/MWRI soil moisture using an artificial neural network based on reconstructed MODIS optical products over the Tibetan Plateau. *Journal of Hydrology, 543*, 242-254

Dai, L., Che, T., Ding, Y., & Hao, X. (2017). Evaluation of snow cover and snow depth on the Qinghai–Tibetan Plateau derived from passive microwave remote sensing. *The Cryosphere, 11*, 1933-1948

Davidson, A., & Wang, S. (2004). The effects of sampling resolution on the surface albedos of dominant land cover types in the North American boreal region. *Remote Sensing of Environment, 93*, 211-224

Dee, D.P., Uppala, S.M., Simmons, A.J., Berrisford, P., Poli, P., Kobayashi, S., Andrae, U., Balmaseda, M., Balsamo, G., & Bauer, d.P. (2011). The ERA‐Interim reanalysis: Configuration and performance of the data assimilation system. *Quarterly Journal of the royal meteorological society, 137*, 553-597

Essery, R., & Pomeroy, J. (2004). Implications of spatial distributions of snow mass and melt rate for snow-cover depletion: theoretical considerations. *Annals of Glaciology, 38*, 261-265

Fang, H., Liang, S., Kim, H.Y., Townshend, J.R., Schaaf, C.L., Strahler, A.H., & Dickinson, R.E. (2007). Developing a spatially continuous 1 km surface albedo data set over North America from Terra MODIS products. *Journal of Geophysical Research: Atmospheres, 112*

Foster, J., Hall, D., Chang, A., & Rango, A. (1984). An overview of passive microwave snow research and results. *Reviews of Geophysics, 22*, 195-208

Foster, J.L., Sun, C., Walker, J.P., Kelly, R., Chang, A., Dong, J., & Powell, H. (2005). Quantifying the uncertainty in passive microwave snow water equivalent observations. *Remote Sensing of Environment, 94*, 187-203

Franch, B., Vermote, E., & Claverie, M. (2014). Intercomparison of Landsat albedo retrieval techniques and evaluation against in situ measurements across the US SURFRAD network. *Remote Sensing of Environment, 152*, 627-637

Freitas, S.C., Trigo, I.F., Macedo, J., Barroso, C., Silva, R., & Perdigão, R. (2013). Land surface temperature from multiple geostationary satellites. *International Journal of remote sensing, 34*, 3051-3068

GCOS, O. (2004). Implementation plan for the global observing system for climate in support of the UNFCCC. *GCOS-92), Geneva*

Gerber, F., de Jong, R., Schaepman, M.E., Schaepman-Strub, G., & Furrer, R. (2018). Predicting missing values in spatio-temporal remote sensing data. *IEEE Transactions on Geoscience and Remote Sensing, 56*, 2841-2853

Guan, B., Molotch, N.P., Waliser, D.E., Fetzer, E.J., & Neiman, P.J. (2010). Extreme snowfall events linked to atmospheric rivers and surface air temperature via satellite measurements. *Geophysical Research Letters, 37*

Guan, X., Huang, J., Guo, N., Bi, J., & Wang, G. (2009). Variability of soil moisture and its relationship with surface albedo and soil thermal parameters over the Loess Plateau. *Advances in Atmospheric Sciences, 26*, 692-700

Gueymard, C.A., Lara-Fanego, V., Sengupta, M., & Xie, Y. (2019). Surface albedo and reflectance: Review of definitions, angular and spectral effects, and intercomparison of major data sources in support of advanced solar irradiance modeling over the Americas. *Solar Energy, 182*, 194-212

Hall, D.K., Riggs, G.A., DiGirolamo, N.E., & Román, M.O. (2019). Evaluation of MODIS and VIIRS cloud-gap-filled snow-cover products for production of an Earth science data record. *Hydrology and Earth System Sciences, 23*, 5227-5241

Hancock, S., Baxter, R., Evans, J., & Huntley, B. (2013). Evaluating global snow water equivalent products for testing land surface models. *Remote Sensing of Environment, 128*, 107-117

Hansen, J., Russell, G., Rind, D., Stone, P., Lacis, A., Lebedeff, S., Ruedy, R., & Travis, L. (1983). Efficient three-dimensional global models for climate studies: Models I and II. *Monthly Weather Review, 111*, 609-662

He, T., Gao, F., Liang, S., & Peng, Y. (2019). Mapping climatological bare soil albedos over the contiguous United States using MODIS data. *Remote Sensing, 11*, 666

He, T., Liang, S., & Song, D.X. (2014). Analysis of global land surface albedo climatology and spatial‐temporal variation during 1981–2010 from multiple satellite products. *Journal of Geophysical Research: Atmospheres, 119*, 10,281-210,298

He, T., Liang, S., Wang, D., Cao, Y., Gao, F., Yu, Y., & Feng, M. (2018). Evaluating land surface albedo estimation from Landsat MSS, TM, ETM+, and OLI data based on the unified direct estimation approach. *Remote Sensing of Environment, 204*, 181-196

He, T., Liang, S., Yu, Y., Wang, D., Gao, F., & Liu, Q. (2013). Greenland surface albedo changes in July 1981–2012 from satellite observations. *Environmental Research Letters, 8*, 044043

Heldens, W., Heiden, U., Esch, T., Mueller, A., & Dech, S. (2017). Integration of remote sensing based surface information into a three-dimensional microclimate model. *ISPRS Journal of Photogrammetry and Remote Sensing, 125*, 106-124

Helfrich, S.R., McNamara, D., Ramsay, B.H., Baldwin, T., & Kasheta, T. (2007). Enhancements to, and forthcoming developments in the Interactive Multisensor Snow and Ice Mapping System (IMS). *Hydrological Processes: An International Journal, 21*, 1576-1586

Hu, Y., Jia, G., Pohl, C., Zhang, X., & van Genderen, J. (2016). Assessing surface albedo change and its induced radiation budget under rapid urbanization with Landsat and GLASS data. *Theoretical and Applied Climatology, 123*, 711-722

Huang, S., Jin, S., Dahal, D., Chen, X., Young, C., Liu, H., & Liu, S. (2013). Reconstructing satellite images to quantify spatially explicit land surface change caused by fires and succession:

A demonstration in the Yukon River Basin of interior Alaska. *ISPRS Journal of Photogrammetry and Remote Sensing, 79*, 94-105

Jääskeläinen, E., Manninen, T., Hakkarainen, J., & Tamminen, J. (2022). Filling gaps of black-sky surface albedo of the Arctic sea ice using gradient boosting and brightness temperature data. *International journal of applied earth observation and geoinformation, 107*, 102701

Jia, A., Liang, S., Jiang, B., Zhang, X., & Wang, G. (2018). Comprehensive Assessment of Global Surface Net Radiation Products and Uncertainty Analysis. *Journal of Geophysical Research Atmospheres, 123*, 1970-1989

Jia, A., Liang, S., & Wang, D. (2022a). Generating a 2-km, all-sky, hourly land surface temperature product from Advanced Baseline Imager data. *Remote Sensing of Environment, 278*, 113105

Jia, A., Liang, S., Wang, D., Jiang, B., & Zhang, X. (2020). Air pollution slows down surface warming over the Tibetan Plateau. *Atmospheric Chemistry and Physics, 20*, 881-899

Jia, A., Liang, S., Wang, D., Ma, L., Wang, Z., & Xu, S. (2022b). Global hourly, 5 km, all-sky land surface temperature data from 2011 to 2021 based on integrating geostationary and polar-orbiting satellite data. *Earth System Science Data Discussions*, 1-35

Jia, A., Ma, H., Liang, S., & Wang, D. (2021). Cloudy-sky land surface temperature from VIIRS and MODIS satellite data using a surface energy balance-based method. *Remote Sensing of Environment, 263*, 112566

Jia, A., Wang, D., Liang, S., Peng, J., & Yu, Y. (2022c). Global daily actual and snow-free blue-sky land surface albedo climatology from 20-year MODIS products. *Journal of Geophysical Research: Atmospheres*, e2021JD035987

Jiang, B., Liang, S.L., Jia, A.L., Xu, J.L., Zhang, X.T., Xiao, Z.Q., Zhao, X., Jia, K., & Yao, Y.J. (2019). Validation of the Surface Daytime Net Radiation Product From Version 4.0 GLASS Product Suite. *IEEE Geoscience and Remote Sensing Letters, 16*, 509-513

Ju, J., Roy, D.P., Shuai, Y., & Schaaf, C. (2010). Development of an approach for generation of temporally complete daily nadir MODIS reflectance time series. *Remote Sensing of Environment, 114*, 1-20

Karlsson, K.-G., Riihelä, A., Müller, R., Meirink, J., Sedlar, J., Stengel, M., Lockhoff, M., Trentmann, J., Kaspar, F., & Hollmann, R. (2013). CLARA-A1: a cloud, albedo, and radiation dataset from 28 yr of global AVHRR data. *Atmospheric Chemistry and Physics, 13*, 5351-5367

Kennedy, R.E., Yang, Z., & Cohen, W.B. (2010). Detecting trends in forest disturbance and recovery using yearly Landsat time series: 1. LandTrendr—Temporal segmentation algorithms. *Remote Sensing of Environment, 114*, 2897-2910

King, M.D., Platnick, S., Menzel, W.P., Ackerman, S.A., & Hubanks, P.A. (2013). Spatial and temporal distribution of clouds observed by MODIS onboard the Terra and Aqua satellites. *IEEE Transactions on Geoscience and Remote Sensing, 51*, 3826-3852

Kostadinov, T.S., Schumer, R., Hausner, M., Bormann, K.J., Gaffney, R., McGwire, K., Painter, T.H., Tyler, S., & Harpold, A.A. (2019). Watershed-scale mapping of fractional snow cover under conifer forest canopy using lidar. *Remote Sensing of Environment, 222*, 34-49

Kumar, S., Mocko, D., Vuyovich, C., & Peters-Lidard, C. (2020). Impact of Surface Albedo Assimilation on Snow Estimation. *Remote Sensing, 12*

Laine, V., Manninen, T., Riihelä, A., & Andersson, K. (2011). Shortwave broadband black-sky surface albedo estimation for Arctic sea ice using passive microwave radiometer data. *Journal of Geophysical Research: Atmospheres, 116*

Lawrence, D., Fisher, R.A., Koven, C.D., Oleson, K.W., Swenson, S.C., Bonan, G., Collier, N., Ghimire, B., Van Kampenhout, L., & Kennedy, D. (2019). The Community Land Model version 5: Description of new features, benchmarking, and impact of forcing uncertainty. *Journal of Advances in Modeling Earth Systems, 11*, 4245-4287

Lawrence, P.J., & Chase, T.N. (2007). Representing a new MODIS consistent land surface in the Community Land Model (CLM 3.0). *Journal of Geophysical Research: Biogeosciences, 112*

Li, X., Jing, Y., Shen, H., & Zhang, L. (2019a). The recent developments in cloud removal approaches of MODIS snow cover product. *Hydrology and Earth System Sciences, 23*, 2401-2416

Li, X., Qu, Y., Lv, M., Song, Y., & Zhao, X. (2021). The Driving Factors of Global Land Surface Albedo: An Analysis with the Glass and Merra-2 Data. In, *2021 IEEE International Geoscience and Remote Sensing Symposium IGARSS* (pp. 6661-6664): IEEE

Li, X., Wang, L., Cheng, Q., Wu, P., Gan, W., & Fang, L. (2019b). Cloud removal in remote sensing images using nonnegative matrix factorization and error correction. *ISPRS Journal of Photogrammetry and Remote Sensing, 148*, 103-113

Li, Y., Wang, T., Zeng, Z., Peng, S., Lian, X., & Piao, S. (2016). Evaluating biases in simulated land surface albedo from CMIP5 global climate models. *Journal of Geophysical Research: Atmospheres, 121*, 6178-6190

Liang, S., Cheng, J., Jia, K., Jiang, B., Liu, Q., Xiao, Z., Yao, Y., Yuan, W., Zhang, X., & Zhao, X. (2021). The global Land surface satellite (GLASS) product suite. *Bulletin of the American Meteorological Society, 102*, E323-E337

Liang, S., Wang, K.C., Zhang, X.T., & Wild, M. (2010). Review on Estimation of Land Surface Radiation and Energy Budgets From Ground Measurement, Remote Sensing and Model Simulations. *IEEE Journal of Selected Topics in Applied Earth Observations and Remote Sensing, 3*, 225-240

Liang, S., Zhao, X., Liu, S., Yuan, W., Cheng, X., Xiao, Z., Zhang, X., Liu, Q., Cheng, J., & Tang, H. (2013). A long-term Global LAnd Surface Satellite (GLASS) data-set for environmental studies. *International Journal of Digital Earth, 6*, 5-33

Liljegren, J.C., Boukabara, S.-A., Cady-Pereira, K., & Clough, S.A. (2005). The effect of the half-width of the 22-GHz water vapor line on retrievals of temperature and water vapor profiles with a 12-channel microwave radiometer. *IEEE Transactions on Geoscience and Remote Sensing, 43*, 1102-1108

Liu, N., Liu, Q., Wang, L., Liang, S., Wen, J., Qu, Y., & Liu, S. (2013a). A statistics-based temporal filter algorithm to map spatiotemporally continuous shortwave albedo from MODIS data. *Hydrology and Earth System Sciences, 17*, 2121-2129

Liu, N., Liu, Q., Wang, L., & Wen, J. (2011). A temporal filtering algorithm to reconstruct daily albedo series based on glass albedo product. In, *Geoscience and Remote Sensing Symposium (IGARSS), 2011 IEEE International* (pp. 4277-4280): IEEE

Liu, Q., Wang, L., Qu, Y., Liu, N., Liu, S., Tang, H., & Liang, S. (2013b). Preliminary evaluation of the long-term GLASS albedo product. *International Journal of Digital Earth, 6*, 69-95

Liu, X., Jiang, L., Wu, S., Hao, S., Wang, G., & Yang, J. (2018). Assessment of methods for passive microwave snow cover mapping using FY-3C/MWRI data in China. *Remote Sensing, 10*, 524

Lucht, W., Schaaf, C.B., & Strahler, A.H. (2000). An algorithm for the retrieval of albedo from space using semiempirical BRDF models. *IEEE Transactions on Geoscience and Remote Sensing, 38*, 977-998

Luojus, K., Pulliainen, J., Takala, M., Lemmetyinen, J., Mortimer, C., Derksen, C., Mudryk, L., Moisander, M., Hiltunen, M., & Smolander, T. (2021). GlobSnow v3. 0 Northern Hemisphere snow water equivalent dataset. *Scientific Data, 8*, 1-16

Meloche, J., Langlois, A., Rutter, N., Royer, A., King, J., Walker, B., Marsh, P., & Wilcox, E.J. (2022). Characterizing tundra snow sub-pixel variability to improve brightness temperature estimation in satellite SWE retrievals. *Cryosphere, 16*, 87-101

Meng, X., Lyu, S., Zhang, T., Zhao, L., Li, Z., Han, B., Li, S., Ma, D., Chen, H., & Ao, Y. (2018). Simulated cold bias being improved by using MODIS time-varying albedo in the Tibetan Plateau in WRF model. *Environmental Research Letters, 13*, 044028

Metsämäki, S., Pulliainen, J., Salminen, M., Luojus, K., Wiesmann, A., Solberg, R., Böttcher, K., Hiltunen, M., & Ripper, E. (2015). Introduction to GlobSnow Snow Extent products with considerations for accuracy assessment. *Remote Sensing of Environment, 156*, 96-108

Moody, E.G., King, M.D., Platnick, S., Schaaf, C.B., & Gao, F. (2005). Spatially complete global spectral surface albedos: Value-added datasets derived from Terra MODIS land products. *IEEE Transactions on Geoscience and Remote Sensing, 43*, 144-158

Moreno-Martinez, A., Izquierdo-Verdiguier, E., Maneta, M.P., Camps-Valls, G., Robinson, N., Munoz-Mari, J., Sedano, F., Clinton, N., & Running, S.W. (2020). Multispectral high resolution sensor fusion for smoothing and gap-filling in the cloud. *Remote Sensing of Environment, 247*

Mortimer, C., Mudryk, L., Derksen, C., Brady, M., Luojus, K., Venäläinen, P., Moisander, M., Lemmetyinen, J., Takala, M., & Tanis, C. (2022). Benchmarking algorithm changes to the Snow CCI+ snow water equivalent product. *Remote Sensing of Environment, 274*, 112988

Mortimer, C., Mudryk, L., Derksen, C., Luojus, K., Brown, R., Kelly, R., & Tedesco, M. (2020). Evaluation of long-term Northern Hemisphere snow water equivalent products. *The Cryosphere, 14*, 1579-1594

Muller, J.-P., López, G., Watson, G., Shane, N., Kennedy, T., Yuen, P., Lewis, P., Fischer, J., Guanter, L., & Domench, C. (2012). The ESA GlobAlbedo Project for mapping the Earth’s land surface albedo for 15 years from European sensors. In, *Geophysical Research Abstracts* (p. 10969)

Muñoz-Sabater, J., Dutra, E., Agustí-Panareda, A., Albergel, C., Arduini, G., Balsamo, G., Boussetta, S., Choulga, M., Harrigan, S., & Hersbach, H. (2021). ERA5-Land: A state-of-the-art global reanalysis dataset for land applications. *Earth System Science Data, 13*, 4349-4383

Orsolini, Y., Wegmann, M., Dutra, E., Liu, B., Balsamo, G., Yang, K., de Rosnay, P., Zhu, C., Wang, W., & Senan, R. (2019). Evaluation of snow depth and snow cover over the Tibetan Plateau in global reanalyses using in situ and satellite remote sensing observations. *The Cryosphere, 13*, 2221-2239

Painter, T.H., Berisford, D.F., Boardman, J.W., Bormann, K.J., Deems, J.S., Gehrke, F., Hedrick, A., Joyce, M., Laidlaw, R., & Marks, D. (2016). The Airborne Snow Observatory: Fusion of scanning lidar, imaging spectrometer, and physically-based modeling for mapping snow water equivalent and snow albedo. *Remote Sensing of Environment, 184*, 139-152

Pan, C.G., Kirchner, P.B., Kimball, J.S., & Du, J.Y. (2020). A Long-Term Passive Microwave Snowoff Record for the Alaska Region 1988-2016. *Remote Sensing, 12*

Pan, H., Wang, J., & Li, H. (2015). Accuracy validation of the MODIS snow albedo products and estimate of the snow albedo under cloud over the Qilian Mountains. *Journal of Glaciology and Geocryology, 37*, 49-57

Peng, J., Yu, P., Yu;, Y., Jia, A., Wang, D., WANG, Z., wang, h., & Liang, S. (2022). An evaluation of the NOAA global daily gap-filled VIIRS surface albedo. *Remote Sensing of Environment, Under Review*

Peng, J., Yu, Y., Jia, A., Wang, D., & Shunlin, L. (2020). Enhancement of snow and ice albedo performance in VIIRS global surface albedo products. In, *AGU Fall Meeting Abstracts* (pp. IN035-0001)

Pistone, K., Eisenman, I., & Ramanathan, V. (2014). Observational determination of albedo decrease caused by vanishing Arctic sea ice. *Proceedings of the National Academy of Sciences, 111*, 3322-3326

Platnick, S., King, M., Meyer, K., Wind, G., Amarasinghe, N., Marchant, B., Arnold, G., Zhang, Z., Hubanks, P., & Ridgway, B. (2015). MODIS atmosphere L3 monthly product. *NASA MODIS Adaptive Processing System, Goddard Space Flight Center, USA, 20*

Qu, Y., Liang, S.L., Liu, Q., He, T., Liu, S.H., & Li, X.W. (2015). Mapping Surface Broadband Albedo from Satellite Observations: A Review of Literatures on Algorithms and Products. *Remote Sensing, 7*, 990-1020

Ramsay, B.H. (1998). The interactive multisensor snow and ice mapping system. *Hydrological Processes, 12*, 1537-1546

Rechid, D., Raddatz, T.J., & Jacob, D. (2009). Parameterization of snow-free land surface albedo as a function of vegetation phenology based on MODIS data and applied in climate modelling. *Theoretical and Applied Climatology, 95*, 245-255

Roerink, G., Menenti, M., & Verhoef, W. (2000). Reconstructing cloudfree NDVI composites using Fourier analysis of time series. *International Journal of remote sensing, 21*, 1911-1917

Rufin, P., Frantz, D., Ernst, S., Rabe, A., Griffiths, P., Özdoğan, M., & Hostert, P. (2019). Mapping cropping practices on a national scale using intra-annual landsat time series binning. *Remote Sensing, 11*, 232

Sabaghy, S., Walker, J.P., Renzullo, L.J., & Jackson, T.J. (2018). Spatially enhanced passive microwave derived soil moisture: Capabilities and opportunities. *Remote Sensing of Environment, 209*, 551-580

Samain, O., Geiger, B., & Roujean, J.-L. (2006). Spectral normalization and fusion of optical sensors for the retrieval of BRDF and albedo: Application to VEGETATION, MODIS, and MERIS data sets. *IEEE Transactions on Geoscience and Remote Sensing, 44*, 3166-3179

San Jose, J., Meirelles, M., Bracho, R., & Nikonova, N. (2001). A comparative analysis of the flooding and fire effects on the energy exchange in a wetland community (Morichal) of the Orinoco Llanos. *Journal of Hydrology, 242*, 228-254

Sarafanov, M., Kazakov, E., Nikitin, N.O., & Kalyuzhnaya, A.V. (2020). A machine learning approach for remote sensing data gap-filling with open-source implementation: an example regarding land surface temperature, surface albedo and NDVI. *Remote Sensing, 12*, 3865

Schaaf, C., Liu, J., Gao, F., & Strahler, A.H. (2011). MODIS albedo and reflectance anisotropy products from Aqua and Terra. *Land Remote Sensing and Global Environmental Change: NASA's Earth Observing System and the Science of ASTER and MODIS, 11*, 549-561

Schaaf, C., Strahler, A., Chopping, M., Gao, F., Hall, D., Jin, Y., Liang, S., Nightingale, J., Román, M., & Roy, D. (2020). MODIS MCD43 product user guide V005. *Boston, MA, USA, Univ. Massachusetts Boston. Accessed: Jul, 11*

Schaaf, C.B., Gao, F., Strahler, A.H., Lucht, W., Li, X., Tsang, T., Strugnell, N.C., Zhang, X., Jin, Y., & Muller, J.-P. (2002). First operational BRDF, albedo nadir reflectance products from MODIS. *Remote Sensing of Environment, 83*, 135-148

Scharlemann, J.P., Benz, D., Hay, S.I., Purse, B.V., Tatem, A.J., Wint, G.W., & Rogers, D.J. (2008). Global data for ecology and epidemiology: a novel algorithm for temporal Fourier processing MODIS data. *PLoS One, 3*, e1408

Schueler, C.F., Clement, J.E., Ardanuy, P.E., Welsch, C., DeLuccia, F., & Swenson, H. (2002). NPOESS VIIRS sensor design overview. In, *Earth Observing Systems VI* (pp. 11-23): SPIE

Sellers, P., Randall, D., Collatz, G., Berry, J., Field, C., Dazlich, D., Zhang, C., Collelo, G., & Bounoua, L. (1996). A revised land surface parameterization (SiB2) for atmospheric GCMs. Part I: Model formulation. *Journal of Climate, 9*, 676-705

Sharifi, E., Saghafian, B., & Steinacker, R. (2019). Downscaling satellite precipitation estimates with multiple linear regression, artificial neural networks, and spline interpolation techniques. *Journal of Geophysical Research: Atmospheres, 124*, 789-805

Shen, H., Li, X., Cheng, Q., Zeng, C., Yang, G., Li, H., & Zhang, L. (2015). Missing information reconstruction of remote sensing data: A technical review. *IEEE Geoscience and Remote Sensing Magazine, 3*, 61-85

Shuai, Y., Masek, J.G., Gao, F., Schaaf, C.B., & He, T. (2014). An approach for the long-term 30-m land surface snow-free albedo retrieval from historic Landsat surface reflectance and MODIS-based a priori anisotropy knowledge. *Remote Sensing of Environment, 152*, 467-479

Sun, D., Li, Y., Zhan, X., Houser, P., Yang, C., Chiu, L., & Yang, R. (2019). Land surface temperature derivation under all sky conditions through integrating AMSR-E/AMSR-2 and MODIS/GOES observations. *Remote Sensing, 11*, 1704

Tao, H., Liang, S., & Song, D.X. (2014). Analysis of global land surface albedo climatology and spatial-temporal variation during 1981–2010 from multiple satellite products. *Journal of Geophysical Research Atmospheres, 119*, 10,281-210,298

Thiebault, K., & Young, S. (2020). Snow cover change and its relationship with land surface temperature and vegetation in northeastern North America from 2000 to 2017. *International Journal of remote sensing, 41*, 8453-8474

Tomar, V., Mandal, V.P., Srivastava, P., Patairiya, S., Singh, K., Ravisankar, N., Subash, N., & Kumar, P. (2014). Rice equivalent crop yield assessment using MODIS sensors' based MOD13A1-NDVI data. *IEEE Sensors Journal, 14*, 3599-3605

Trenberth, K.E., Fasullo, J.T., & Kiehl, J. (2009). Earth's global energy budget. *Bulletin of the American Meteorological Society, 90*, 311-324

Urraca, R., Lanconelli, C., Cappucci, F., & Gobron, N. (2022). Comparison of Long-Term Albedo Products against Spatially Representative Stations over Snow. *Remote Sensing, 14*, 3745

Vander Jagt, B.J., Durand, M.T., Margulis, S.A., Kim, E.J., & Molotch, N.P. (2013). The effect of spatial variability on the sensitivity of passive microwave measurements to snow water equivalent. *Remote Sensing of Environment, 136*, 163-179

Wang, D., Liang, S., He, T., & Yu, Y. (2013). Direct estimation of land surface albedo from VIIRS data: Algorithm improvement and preliminary validation. *Journal of Geophysical Research: Atmospheres, 118*, 12,577-512,586

Wang, D., Liang, S., He, T., Yu, Y., Schaaf, C., & Wang, Z. (2015). Estimating daily mean land surface albedo from MODIS data. *Journal of Geophysical Research: Atmospheres, 120*, 4825-4841

Wang, D., Liang, S., Li, R., & Jia, A. (2021). A synergic study on estimating surface downward shortwave radiation from satellite data. *Remote Sensing of Environment, 264*, 112639

Wang, D., Liang, S., Zhou, Y., He, T., & Yu, Y. (2017). A New Method for Retrieving Daily Land Surface Albedo From VIIRS Data. *IEEE Transactions on Geoscience and Remote Sensing, 55*, 1765-1775

Wang, Q., Wang, L., Zhu, X., Ge, Y., Tong, X., & Atkinson, P.M. (2022). Remote sensing image gap filling based on spatial-spectral random forests. *Science of Remote Sensing*, 100048

Wang, Z.S., Schaaf, C.B., Strahler, A.H., Chopping, M.J., Roman, M.O., Shuai, Y.M., Woodcock, C.E., Hollinger, D.Y., & Fitzjarrald, D.R. (2014). Evaluation of MODIS albedo product (MCD43A) over grassland, agriculture and forest surface types during dormant and snow-covered periods. *Remote Sensing of Environment, 140*, 60-77

Welch, G., & Bishop, G. (1995). An introduction to the Kalman filter

Wu, C.F., Wu, J.P., Luo, Y.M., Zhang, H.B., Teng, Y., & DeGloria, S.D. (2011). Spatial interpolation of severely skewed data with several peak values by the approach integrating kriging and triangular irregular network interpolation. *Environmental Earth Sciences, 63*, 1093-1103

Wu, P., Su, Y., Duan, S.-b., Li, X., Yang, H., Zeng, C., Ma, X., Wu, Y., & Shen, H. (2022). A two-step deep learning framework for mapping gapless all-weather land surface temperature using thermal infrared and passive microwave data. *Remote Sensing of Environment, 277*, 113070

Wu, P., Yin, Z., Yang, H., Wu, Y., & Ma, X. (2019). Reconstructing Geostationary Satellite Land Surface Temperature Imagery Based on a Multiscale Feature Connected Convolutional Neural Network. *Remote Sensing, 11*, 300

Xiao, X., He, T., Liang, S., & Zhao, T. (2021a). Improving fractional snow cover retrieval from passive microwave data using a radiative transfer model and machine learning method. *IEEE Transactions on Geoscience and Remote Sensing*

Xiao, X., Liang, S., He, T., Wu, D., Pei, C., & Gong, J. (2021b). Estimating fractional snow cover from passive microwave brightness temperature data using MODIS snow cover product over North America. *The Cryosphere, 15*, 835-861

Xiao, Z., Liang, S., Wang, J., Jiang, B., & Li, X. (2011). Real-time retrieval of Leaf Area Index from MODIS time series data. *Remote Sensing of Environment, 115*, 97-106

Xu, J.H., & Shu, H. (2014). Assimilating MODIS-based albedo and snow cover fraction into the Common Land Model to improve snow depth simulation with direct insertion and deterministic ensemble Kalman filter methods. *Journal of Geophysical Research-Atmospheres, 119*, 10684-10701

Xu, S., & Cheng, J. (2021). A new land surface temperature fusion strategy based on cumulative distribution function matching and multiresolution Kalman filtering. *Remote Sensing of Environment, 254*, 112256

Xue, H., Wang, J., Xiao, Z., Chen, P., & Liu, Y. (2014). Combining MODIS and AMSR-E observations to improve MCD43A3 short-time snow-covered Albedo estimation. *Hydrological Processes, 28*, 570-580

Yan, L., & Roy, D.P. (2018). Large-area gap filling of Landsat reflectance time series by spectral-angle-mapper based spatio-temporal similarity (SAMSTS). *Remote Sensing, 10*, 609

Yan, L., & Roy, D.P. (2020). Spatially and temporally complete Landsat reflectance time series modelling: The fill-and-fit approach. *Remote Sensing of Environment, 241*, 111718

Yang, J., & Hu, M. (2018). Filling the missing data gaps of daily MODIS AOD using spatiotemporal interpolation. *Science of the Total Environment, 633*, 677-683

Yang, Z.-L., Dickinson, R.E., Robock, A., & Vinnikov, K.Y. (1997). Validation of the snow submodel of the biosphere–atmosphere transfer scheme with Russian snow cover and meteorological observational data. *Journal of Climate, 10*, 353-373

Yu, Y. (2022). STAR Joint Polar Satellite System Website. In. https://www.star.nesdis.noaa.gov/jpss/albedo.php

Zhang, F., Zhang, M., & Poterjoy, J. (2013). E3DVar: Coupling an ensemble Kalman filter with three-dimensional variational data assimilation in a limited-area weather prediction model and comparison to E4DVar. *Monthly Weather Review, 141*, 900-917

Zhang, Q., Yuan, Q., Li, J., Li, Z., Shen, H., & Zhang, L. (2020a). Thick cloud and cloud shadow removal in multitemporal imagery using progressively spatio-temporal patch group deep learning. *ISPRS Journal of Photogrammetry and Remote Sensing, 162*, 148-160

Zhang, Q., Yuan, Q., Zeng, C., Li, X., & Wei, Y. (2018). Missing data reconstruction in remote sensing image with a unified spatial–temporal–spectral deep convolutional neural network. *IEEE Transactions on Geoscience and Remote Sensing, 56*, 4274-4288

Zhang, R., Wang, H., Fu, Q., Rasch, P.J., & Wang, X. (2019a). Unraveling driving forces explaining significant reduction in satellite-inferred Arctic surface albedo since the 1980s. *Proceedings of the National Academy of Sciences, 116*, 23947-23953

Zhang, X., Zhou, J., Gottsche, F.-M., Zhan, W., Liu, S., & Cao, R. (2019b). A Method Based on Temporal Component Decomposition for Estimating 1-km All-Weather Land Surface Temperature by Merging Satellite Thermal Infrared and Passive Microwave Observations. *IEEE Transactions on Geoscience and Remote Sensing, 57*, 4670-4691

Zhang, X., Zhou, J., Liang, S., Chai, L., Wang, D., & Liu, J. (2020b). Estimation of 1-km all-weather remotely sensed land surface temperature based on reconstructed spatial-seamless satellite passive microwave brightness temperature and thermal infrared data. *ISPRS Journal of Photogrammetry and Remote Sensing, 167*, 321-344

Zhou, Y., Wang, D., Liang, S., Yu, Y., & He, T. (2016). Assessment of the Suomi NPP VIIRS land surface albedo data using station measurements and high-resolution albedo maps. *Remote Sensing, 8*, 137